MNRAS **000**, 1–19 (2020) Preprint 15 July 2020 Compiled using MNRAS LaTeX style file v3.0

Seeding the second star — II. CEMP star formation enriched from faint supernovae

Gen Chiaki[1⋆], John H. Wise[1], Stefania Marassi[2], Raffaella Schneider[2,3,4], Marco Limongi[5,6,7], and Alessandro Chieffi[7,8,9]
[1] *Center for Relativistic Astrophysics, School of Physics, Georgia Institute of Technology, Atlanta, GA 30332, USA*
[2] *Dipartimento di Fisica, "Sapienza" Universitàdi Roma, Piazzale Aldo Moro 5, 00185 Roma, Italy*
[3] *INAF/Osservatorio Astronomico di Roma, Via di Frascati 33, 00040 Monte Porzio Catone, Italy*
[4] *INFN, Sezione Roma1, Dipartimento di Fisica, "Sapienza" Universitàdi Roma, Piazzale Aldo Moro 5, 00185, Roma, Italy*
[5] *Istituto Nazionale di Astrofisica - Osservatorio Astronomico di Roma, Via Frascati 33, I-00040, Monteporzio Catone, Italy*
[6] *Kavli Institute for the Physics and Mathematics of the Universe, Todai Institutes for Advanced Study, the University of Tokyo,Kashiwa, Japan 277-8583 (Kavli IPMU, WPI)*
[7] *INFN - Sezione di Perugia, via A. Pascoli, Perugia, Italy*
[8] *Istituto di Astrofisica e Planetologia Spaziali, INAF, via Fosso del cavaliere 100, 00133 Roma, Italy*
[9] *Monash Centre for Astrophysics (MoCA), School of Mathematical Sciences, Monash University, Victoria 3800, Australia*

ABSTRACT

Carbon-enhanced metal-poor (CEMP) stars are the living fossils holding records of chemical enrichment from early generations of stars. In this work, we perform a set of numerical simulations of the enrichment from a supernova (SN) of a first generation of metal-free (Pop III) star and the gravitational collapse of the enriched cloud, considering all relevant cooling/heating processes and chemical reactions as well as the growth of dust grains. We adopt faint SN models for the first time with progenitor masses $M_{\rm PopIII} = 13$–$80\ {\rm M}_{\odot}$, which yield C-enhanced abundance patterns ([C/Fe] = 4.57–4.75) through mixing and fallback of innermost layers of the ejecta. This model also considers the formation and destruction of dust grains. We find that the metals ejected by the SN can be partly re-accreted by the same dark matter minihalo, and carbon abundance of the enriched cloud $A({\rm C}) = 3.80$–5.06 is lower than the abundance range of observed CEMP stars ($A({\rm C}) \gtrsim 6$) because the mass of the metals ejected by faint SNe is smaller than normal core-collapse SNe due to extensive fallback. We also find that cloud fragmentation is induced by gas cooling from carbonaceous grains for $M_{\rm PopIII} = 13\ {\rm M}_{\odot}$ even with the lowest iron abundance $[{\rm Fe/H}] \sim -9$. This leads to the formation of low-mass stars, and these "giga metal-poor" stars can survive until the present-day Universe and may be found by future observations.

Key words: galaxies: evolution — ISM: abundances — stars: formation — stars: low-mass — stars: Population III — stars: Population II

1 INTRODUCTION

Metal-poor stars are important astronomical objects that hold the signatures of chemical abundance in the early phase of metal enrichment in the Universe. In particular, extremely metal-poor (EMP) stars with metallicities $[{\rm Fe/H}] < -3$ are considered to form in gas clouds enriched by only a few progenitors (Audouze & Silk 1995; Ryan et al. 1996; Cayrel et al. 2004).[1] Inversely, we can indirectly see the nucleosynthesis of the progenitors from the metallicities and elemental abundances of EMP stars. This approach to chemical evolution in the early Universe is called *galactic archaeology* (Salvadori et al. 2007; de Bennassuti et al. 2014, 2017; Graziani et al. 2015; Hartwig et al. 2018; Komiya et al. 2020). Also, for the ancient stars to be observed in the present day, they should be low-mass ($< 0.8\ {\rm M}_{\odot}$). The metallicity distribu-

---

⋆ E-mail: gen.chiaki@physics.gatech.edu

[1] The logarithmic number abundance ratio between elements A and B relative to solar one $[{\rm A/B}] = \log(n_{\rm A}/n_{\rm B}) - \log(n_{\rm A}/n_{\rm B})_{\odot}$ is often used to measure the metal content and peculiarity of elemental abundance ratio of a star. We also use the logarithmic abundance $A({\rm M}) = \log \epsilon({\rm M}) = 12 + \log(n_{\rm M}/n_{\rm H})$ of an element M. We hereafter use the solar abundance of Asplund et al. (2009).

tion of EMP stars gives a constraint on their initial mass functions (IMFs) with different metallicities.

Another important aim of this study is to search for the first generation of metal-free (Population III or Pop III) stars that first modify cosmic structure formation through their radiative and SN feedback. So far, metal-free stars have not been observed although a large number (~ 5000) of metal-poor stars have been identified in the Milky Way halo and Local Group dwarf galaxies in large survey campaigns and follow-up spectroscopic observations. This indicates that Pop III stars are predominantly massive. Numerical studies (Bromm et al. 1999; Abel et al. 2002; Yoshida et al. 2003) also predict that massive Pop III stars with $M_{\rm PopIII} \sim 10$–$1000\ {\rm M_{\odot}}$ form in the metal-free gas clouds hosted by low-mass ($\sim 10^6\ {\rm M_{\odot}}$) dark matter (DM) halos (minihalos; MHs) at redshift $z \gtrsim 6$. The fragmentation of the pristine clouds is significantly reduced due to the lack of efficient gas coolants.

On the other hand, the survival of stars with non-zero metallicities indicates that the additional gas cooling due to heavy elements induces the fragmentation of their parent clouds. In particular, thermal emission cooling of dust grains becomes dominant at high densities $n_{\rm H} \sim 10^{12}$–$10^{14}\ {\rm cm^{-3}}$, corresponding to small Jeans masses $M_{\rm J} \sim 0.01$–$0.1\ {\rm M_{\odot}}$, which may be indicative of low-mass star formation (Omukai 2000; Omukai et al. 2005; Schneider et al. 2002, 2003, 2006, 2012a). Several authors have studied dust-induced fragmentation, but they assume that the metal-poor clouds have the solar elemental abundance ratio and the same composition and size distribution of grains as in the local interstellar medium (ISM) (Omukai 2000; Ritter et al. 2015; Smith et al. 2015; Safranek-Shrader et al. 2016) (see however Schneider et al. 2006).

Following the discovery of the EMP star SDSS J1029+1729 by Caffau et al. (2011), with a total metallicity of only $Z = 4.5 \times 10^{-5}\ {\rm Z_{\odot}}$, Schneider et al. (2012b) showed that its surface elemental abundances suggest that its birth cloud was enriched by the metal and dust yields of normal core-collapse SNe (CCSNe) and that the gas cooled through silicate dust cooling and fragmented. The same method was then applied by Marassi et al. (2015) to investigate the origin of SMSS J0313−6708, a carbon-enhanced star with an upper limit on its surface iron abundance of only $[{\rm Fe/H}] < -7.1$ (Keller et al. 2014). It was suggested that, similarly to other carbon enhanced metal-poor (CEMP) stars with $[{\rm Fe/H}] \lesssim -3$ (so-called Group II and III of CEMP stars; Yoon et al. 2016),[2] this star could originate from dust-cooling and fragmentation of a collapsing gas cloud previously enriched by the yields of faint SNe. In faint SNe, mixing and fall back of the innermost layers of the ejecta into the central compact remnant can yield the C-enhanced abundance pattern of ejected materials. Since ^{56}Ni, main source of γ-ray photons through its radioactive decay, is also depleted, this type of SNe is called faint SNe (Umeda & Nomoto 2003). In addition, Marassi et al. (2014, 2015) show that the carbonaceous grains are produced from faint SNe and could be responsible for the formation of SMSS J0313 − 6708. Hence, it was suggested that the distinctive elemental abundances between C-normal and C-enhanced EMP stars point to a different type of SN explosion as the main formation sites of their surface elemental abundance, but to a common formation pathway based on either silicates or carbon dust cooling (Marassi et al. 2015). This scenario was further investigated by Chiaki et al. (2017), who showed that the observed lower-limits of carbon abundance $A_{\rm cr}({\rm C}) \sim 6$ for CEMP (for reference, the solar abundance is $A_{\odot}({\rm C}) = 8.43$; Asplund et al. 2009) and of iron abundance of $[{\rm Fe/H}]_{\rm cr} \sim -5$ for C-normal EMP (CN-EMP) stars confirm that gas cooling by dust driven cooling and fragmentation in their birth clouds is required, and that the dominant grain species are carbon and silicates, respectively.

Although these models successfully reproduce the *relative* element-to-element abundances of observed stars, the studies for the *absolute* abundance of metals/grains in enriched clouds have so far been limited to normal CCSNe. In our previous study (Chiaki & Wise 2019, hereafter Paper I), we followed the metal enrichment from a normal CCSN with $[{\rm C/Fe}] = 0.18$. We found that only a fraction $f_{\rm ret} \sim 0.4\%$ of metals return to the MH because the SN shell interacts with dense cosmological filaments and loses its energy through radiative cooling. Still, the metallicity of an enriched cloud $[{\rm Fe/H}] = -3.62$ is consistent with the metallicity range of observed C-normal stars.[3] Mainly silicate grains ejected from the SN induce gas cooling in the enriched cloud and fragmentation occurs. Hence, the scenario proposed in Paper I could explain the origin of C-normal stars from a single CCSN.

For faint SNe, the ejected metal mass is smaller than for normal CCSNe because the ejecta partially falls back. Also, faint SNe exploding in a spherically symmetric manner have smaller explosion energies than normal CCSNe with the same progenitor mass. This can affect the return fraction of metals $f_{\rm ret}$. Therefore, it is necessary to investigate whether the enriched clouds have C abundances consistent with the observed level ($A({\rm C}) \gtrsim 6$).

In the present study, we follow the metal enrichment from a faint SN and the gravitational collapse of an enriched cloud with a set of cosmological simulations. To quantify the absolute metal and dust abundances in the enriched cloud, for the first time we employ a nucleosynthesis/nucleation model of Pop III faint SNe produced by Marassi et al. (2014, hereafter M14). The metal mass and explosion energy are consistently derived so that the model reproduces the elemental abundance of the CEMP star SMSS J0313 − 6708 (Keller et al. 2014) for given progenitor masses. We then follow the gravitational collapse of the enriched cloud with

---

[2] Instead, Group I stars are distributed mostly at intermediate metallicities, with $[{\rm Fe/H}] \sim -2$, and show also s-process element enhancement. Because of this, their carbon-enhancement is believed to originate from mass transfer from an AGB companion in a binary system (Suda et al. 2004). Alternatively, Group I stars could form in regions that have been previously enriched by the explosion of rotating massive stars, that could produce C/N and s-process elements in their envelopes (Meynet et al. 2006; Choplin, Tominaga & Ishigaki 2019).

[3] In Paper I, we presented the iron abundance of the recollapsing cloud as $[{\rm Fe/H}] = -3.42$. In the simulation, we used the solar metallicity $Z_{\odot} = 0.01295$ as in this work, and the metallicity of the recollapsing cloud was $Z = 3.4 \times 10^{-6} = 2.6 \times 10^{-4}\ {\rm Z_{\odot}}$. However, when we converted Z from $[{\rm Fe/H}] = 12 + \log(X({\rm Fe})Z/\mu_{\rm Fe}X_{\rm H}) - A_{\odot}({\rm Fe})$, we used ${\rm Z_{\odot}} = 0.02$. If we use ${\rm Z_{\odot}} = 0.01295$, [Fe/H] is consistently estimated to be −3.62.

all relevant cooling/heating processes including carbon grain cooling and chemical reactions as well as growth of dust grains (Chiaki et al. 2015) to determine whether the gas cloud is able to fragment, allowing the formation of low-mass and long-lived stars, such as SMSS J0313 − 6708.

The structure of this paper is as follows: In Section 2, we describe our numerical methods. Then, the results are presented in Section 3. We discuss the observability of stars forming in the simulated clouds enriched by faint SNe and other issues in Section 4. Finally, the paper is concluded in Section 5. Throughout the simulations, we adopt the cosmological parameters $\Omega_{\rm m} = 0.3089$, $\Omega_{\rm CDM} = 0.2603$, $\Omega_\Lambda = 0.6911$, and $H_0 = 67.74$ km s^{-1} Mpc^{-1} (Planck Collaboration et al. 2016). We run the simulations in comoving coordinates but we describe physical quantities in proper coordinates throughout this paper, unless otherwise specified. All the figures in this paper are created with the YT toolkit (Turk et al. 2011).[4]

2 NUMERICAL MODELS

Since the numerical method is nearly the same as Paper I, we briefly describe it in Sections 2.1 and 2.2. We detail a faint SN model that is, for the first time, included in three-dimensional simulations of this work in Section 2.3.

2.1 Basic setup

We perform cosmological simulations with the adaptive mesh refinement (AMR) hydrodynamics code ENZO (Bryan et al. 2014).[5] The dynamics of DM is followed with an N-body particle-mesh solver (Efstathiou et al. 1985; Bryan & Norman 1997). The hydrodynamics equations are solved with the piecewise parabolic method (PPM) in an Eulerian frame (Woodward & Colella 1984; Bryan et al. 1995) and a Harten-Lax-van Leer-Contact (HLLC) Riemann solver, which accurately captures hydrodynamical shocks and computes advection of chemical species across contact discontinuities. We set the controlling parameters for the flux calculation and interpolation of field values between computational grids as `FluxCorrection` = 2 and `ConservativeInterpolation` = 0 to minimize numerical errors. Although errors for the total metal mass accumulates up to ∼ 7% at ∼ 500 Myr after a SN explosion even with the above setting, this is below the typical observational error of stellar abundances (∼ 0.1 dex).

Computational cells are progressively refined by a factor of two in space when satisfying the following criteria:

(i) The baryon mass in a cell exceeds $3m_{\rm b,0} \times 2^{-0.2l}$ on a refinement level l, where $m_{\rm b,0}$ is the mean baryon mass on the root grid.

(ii) The DM particle mass contained by a cell exceeds $3m_{\rm dm,0}$, where $m_{\rm dm,0}$ is the mean DM mass on the root grid.

(iii) The local Jeans length $\lambda_{\rm J}$ is resolved less than 64 cells.

The negative coefficient −0.2 in the spectral index of the criterion means (i) the super-Lagrangian refinement criterion for the gas component while the criterion (ii) the Lagrangian for the DM. When the baryon density starts to increase in the run-away collapse phase, cells are refined mostly on the criterion (iii). This criterion warranties that the local Jeans length is resolved sufficiently to prevent spurious fragmentation (Truelove et al. 1997; Turk et al. 2012).

We generate the initial conditions of the simulations in a periodic box with a side of 300 kpc (comoving) with MUSIC (Hahn & Abel 2011). We initially run a DM-only simulation with a base resolution 64^3 and identify the most massive halo with a mass 3.8×10^6 M$_\odot$ at redshift $z = 10$ with a friends-of-friends (FOF) algorithm. By initially refining the halo region with two additional AMR levels, i.e., with higher spatial resolution by a factor of four, we restart the simulation adding the baryon component. With this zoom-in strategy, the effective resolution is 256^3 and the minimum DM particle mass is 53.4 M$_\odot$.

2.2 Simulations of CEMP star formation

In this section, we describe the numerical methods that follow the formation of a Pop III star (Section 2.2.1), its radiative and SN feedback (Section 2.2.2), and recollapse of an enriched cloud in the MH (Section 2.2.3).

2.2.1 Pop III star formation

The main coolant of a primordial cloud is hydrogen molecules (H_2) and, in some cases, hydrogen deuteride molecules (HD). To calculate the fractions and cooling rates of H_2 and HD, we solve the non-equilibrium chemistry with a modified version of a chemistry/cooling library GRACKLE (Smith et al. 2017, Paper I).[6] We solve a chemical network of 49 reactions for 15 primordial species, e^-, H^+, H, H^-, H_2^+, H_2, D^+, D, D^-, HD^+, HD, He, He^+, He^{2+}, and HeH^+. This chemical network includes the collisional ionization/recombination of H/He and formation/dissociation of H_2/HD molecules. We compute the rates of radiative cooling: inverse Compton, bremsstrahlung, H/He line transition, H_2 ro-vibrational transition, and HD rotational transition cooling. When H_2 molecules form, the binding energy (4.48 eV per molecule) is converted to the thermal energy (see Omukai 2000). The continuum opacity $\kappa_{\rm p}$ of the primordial component is taken from Mayer & Duschl (2005). Throughout this paper, the mass fraction of hydrogen nuclei is $X_{\rm H} = 0.76$ and number fraction of deuterium relative to hydrogen nuclei is $y_{\rm D} = 3.4 \times 10^{-5}$.

We then simulate the formation of a Pop III star. In reality, a star forms from a hydrostatic core with a central

---

[4] `https://yt-project.org/`. The version and the script used in this work are respectively available at
`https://github.com/genchiaki/yt/tree/metal-dust`,
`https://github.com/genchiaki/Analysis_CEMP`.
The simulation data will be shared on reasonable request to the authors.

[5] `http://enzo-project.org/`.
The version used in this work is available at
`https://github.com/genchiaki/enzo-dev/tree/metal-dust`.

[6] `https://grackle.readthedocs.io/`.
The version used in this work is available at
`https://github.com/genchiaki/grackle/tree/metal-dust`.

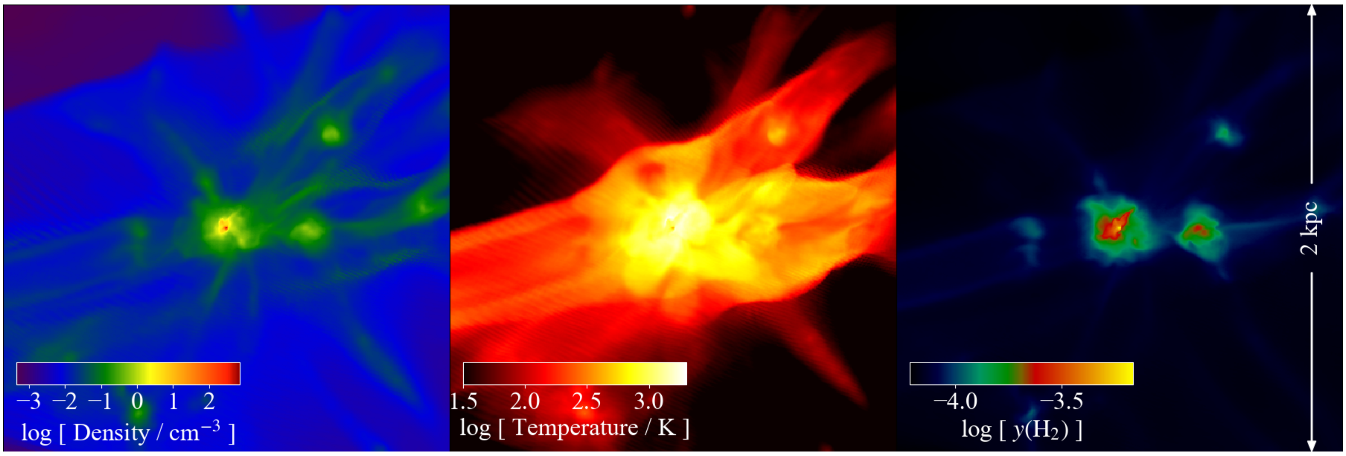

Figure 1. Density-weighted projection of density, temperature, and H_2 abundance of the minihalo just before Pop III star formation (redshift $z = 12.1$) in a box with a side 1 kpc centered on the density maximum. The horizontal and vertical axes are respectively parallel to the major and minor axes of the momentum of inertia of the region with densities above 0.1 cm^{-3}.

density $n_{\rm H} \sim 10^{19}$ cm^{-3} where gas cooling from the endothermic reaction of hydrogen molecular dissociation becomes ineffective (Larson 1969; Penston 1969). In this work, to save the computational cost, we put a Pop III star particle, representing a single star, with the criteria:

(i) gas density exceeds 10^6 cm^{-3},
(ii) gas flow is convergent ($\nabla \cdot \boldsymbol{v} < 0$),
(iii) the cooling time is less than the dynamical time,
(iv) H_2 fraction exceeds a critical value (10^{-3}).

Fig. 1 shows the snapshot of the MH just before the time $t_{\rm form}$ of Pop III star formation. At this time ($z = 12.1$), the DM and baryon mass is $M_{\rm halo,dm} = 1.53 \times 10^6$ M$_\odot$ and $M_{\rm halo,b} = 2.57 \times 10^5$ M$_\odot$, respectively, within the virial radius $R_{\rm halo} = 288$ pc. The H_2 fraction reaches $\sim 10^{-3}$ through the H$^-$ process (Omukai 2000) and the temperature at the center decreases because of H_2 cooling. In this region, the above criteria for Pop III star formation are satisfied.

From the time $t_{\rm form}$, we run three simulations, in each of which we put a single Pop III star with masses 13.5, 50, and 80 M$_\odot$ in the MH (hereafter called the run `F13`, `F50`, and `F80`, respectively).

2.2.2 *Radiation and supernova feedback from a Pop III star*

During the main sequence of the Pop III star, we solve the radiative transfer with a module MORAY (Wise & Abel 2011). The ionization photon emission rate Q(H) and the lifetime of the stars $t_{\rm life}$ are taken from Schaerer (2002) and reported in Table 1. We calculate the H, He, and He$^+$ ionization rates by integrating the number of photons consumed by the atoms from the location of the star particle to each computational cell with the cross-section of Verner et al. (1996). The H_2 dissociation rate is computed from the column density of H_2 with a self-shielding function of Draine & Bertoldi (1996). With these rates, the photon reactions are consistently calculated, coupled with the non-radiative reactions.

After the time $t_{\rm life}$, we uniformly add explosion energy and metals within a sphere with a radius $R_{\rm sh} = 10$ pc centered on the star particle, mimicking the end of the free-expansion phase. We assume that the explosion energy has been completely converted to the thermal energy. We also assume that the ejecta has been completely mixed during the free-expansion phase and its elemental composition is uniform. The explosion energy $E_{\rm SN}$ and mass of ejected metals/grains of our models are described in Section 2.3 and listed in Table 2.

Table 1. Pop III models

^{1}Run	$^2M_{\rm PopIII}$ [M$_\odot$]	$^3t_{\rm life}$ [Myr]	^4Q(H) [10^{48} s^{-1}]
`F13`	13.5	11.8	1.09
`F50`	50	3.49	34.6
`F80`	80	3.03	84.9

Note — (1) ID of runs. (2–4) mass, lifetime, and ionizing photon emission rate of our Pop III star models.

2.2.3 *Collapse of the enriched clouds*

To include the chemical/thermal evolution of clouds enriched by faint SNe, we solve 40 reactions of 19 metal species: C$^+$, C, CH, CH$_2$, CO$^+$, CO, CO$_2$, O$^+$, O, OH$^+$, OH, H$_2$O$^+$, H$_2$O, H$_3$O$^+$, O$_2^+$, O$_2$, Si, SiO, and SiO$_2$. In our cooling model, we include C II, C I, and O I fine-structure transition line cooling and CO, OH, and H$_2$O molecular rotational transition line cooling. The optical depth in each transition line is calculated with the Sobolev length approximation. To reduce the computational cost, we estimate the local velocity gradient to be $|\nabla \cdot \boldsymbol{v}| = 1/3t_{\rm ff}$, where $t_{\rm ff} = (3\pi/32G\rho)^{1/2}$ is the free-fall time for a density ρ (Omukai 2000).

We model the chemistry and cooling of dust grains most carefully. In this work, we consider 7 grain species: alumina (Al$_2$O$_3$), metallic iron (Fe), magnetite (Fe$_3$O$_4$), enstatite (MgSiO$_3$), forsterite (Mg$_2$SiO$_4$), amorphous carbon (AC), and silica (SiO$_2$) with arbitrary grain size distributions. Further, we include grain growth (accretion of gas-phase met-

Table 2. SN models

^{1}Run	$^{2}E_{\rm SN}$ [10^{51} erg]	$^{3}M_{\rm cut}$ [$M_{\odot}$]	$^{4}M_{\rm met}$ [$M_{\odot}$]	$^{5}M_{\rm C}$ [$M_{\odot}$]	$^{6}M_{\rm O}$ [$M_{\odot}$]	$^{7}M_{\rm Fe}$ [$M_{\odot}$]	^{8}[C/Fe]	$^{9}M_{\rm AC}$ [$M_{\odot}$]	$^{10}\mathcal{D}_{\rm AC}$	$^{11}r_{\rm AC,cool}$ [μm]
`F13`	0.5	1.7	0.119	0.079	0.039	1.06×10^{-6}	4.62	1.70×10^{-2}	1.49×10^{-8}	0.096
`F50`	2.6	11	3.54	0.989	2.551	1.47×10^{-5}	4.57	3.89×10^{-4}	4.11×10^{-10}	0.012
`F80`	5.2	22.5	4.31	1.089	3.213	1.05×10^{-5}	4.75	3.74×10^{-2}	2.51×10^{-8}	0.064

Note — (1) ID of runs. (2) explosion energy. (3) mass cut. (4–7) metal, carbon, oxygen, and iron mass in ejecta. (8) carbon-to-iron abundance ratio. (9) mass of amorphous carbon (AC). (10) mass ratio of AC to gas. (11) characteristic radius of AC grains (see text).

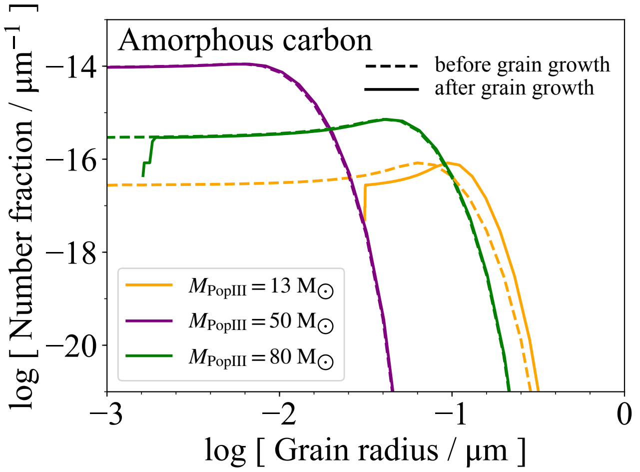

Figure 2. Distribution of the number fraction of amorphous carbon (AC) grains relative to hydrogen nuclei against grain radii in the clouds enriched by Pop III SNe with progenitor masses 13 $M_{\odot}$ (orange), 50 $M_{\odot}$ (purple) and 80 $M_{\odot}$ (green). The dashed and solid curves denote the size distribution of grains in envelope and center of the clouds before and after grain growth occurs, respectively.

als onto grains) as chemical reactions with a reaction rate given by the geometrical cross-section of the grains multiplied by the thermal velocity of metal molecules (Kozasa & Hasegawa 1987). The cooling rates, H_2 formation rates on grain surfaces, continuum opacity, and grain growth rates are calculated for each species. We calculate the continuum optical depth as $\tau_{\rm cont} = (\kappa_{\rm p}\rho + \sum_i \kappa_i \rho_i)\lambda_{\rm J}$ with an opacity κ_i (Nozawa et al. 2008) and density ρ_i of a grain species i.

We terminate the simulations at a density $n_{\rm H} \sim 10^{16}$ cm^{-3} above which further cloud fragmentation does not occur. In this optically thick region, radiative cooling becomes ineffective, and thus stable hydrostatic cores (first cores) form (Larson 1969).

We run the simulations on the PACE cluster in Georgia Institute of Technology on 3 nodes, using 28 cores/node. The maximum AMR level eventually reaches 32–34, corresponding to a spatial size of ~ 0.01 au. Even protostars with a size ~ 1 au can be resolved. The runs `F13`, `F50`, and `F80` take 69, 47, and 41 days with total computational costs of 140,000, 94,000, and 83,000 core-hours, respectively.

2.3 SN models

We adopt faint SN models calculated by M14. In these models, explosion energy $E_{\rm SN}$, ^{56}Ni mass, and initial ejection velocity are chosen so that the abundance ratios of heavy elements are fitted with the elemental abundance of the most iron-poor CEMP star, SMSS J0313 − 6708 (Keller et al. 2014), for each progenitor mass. The mass cut, $M_{\rm cut}$, depends on the initial ejection velocity. The total mass of synthesized metals, $M_{\rm met}$, is 0.119–4.31 $M_{\odot}$. Because of the fall back of the inner layers of the ejecta, the metal mass 0.119 $M_{\odot}$ for `F13` is smaller than that of normal CCSNe with the same progenitor mass (0.3–1 $M_{\odot}$). The masses of C, O, and Fe range between 0.079–1.089 $M_{\odot}$, 0.039–3.213 $M_{\odot}$, and 1.06×10^{-6}–1.05×10^{-5} $M_{\odot}$, respectively. This gives a C-enhanced abundance ratio of [C/Fe] = 4.57–4.75. In these spherical explosion models, the explosion energy for `F13` is smaller (0.5×10^{51} erg) than the normal CCSN model with the same progenitor mass used in Paper I by a factor of two.

M14 follow the formation/destruction of dust grains in faint SNe. First, dust grains form in the expanding ejecta at the time ~ 100 days after the SN explosion. At the time when gas temperature decreases below the sublimation temperature of grains (~ 2000 K), seed clusters form through aggregation of monomers and grow by accreting the gas-phase species. In C-rich ejecta, AC is the dominant species while the mass fraction of other species is at most 10^{-5}. The newly formed grains have an approximately log-normal size distribution function with a mean radius that depends on the C density and temperature at the grain formation time. Then, M14 follow the destruction of dust grains in SN remnants. When the ejecta sweeps up the circumstellar gas with a mass comparable to the ejecta mass, reverse shocks propagate to the region where grains have formed. Through the collision of high energy ions, a fraction of the atoms on grain surfaces returns to the gas phase. Dust destruction occurs at ~ 1000 years after the SNe. This should occur in the three-dimensional simulations but we do not include the dust destruction to save the numerical cost. Instead, we use the dust model of M14 as an initial condition.

The efficiency of grain destruction depends on the density $\rho_{\rm amb}$ of ambient gas around a SN. M14 calculate the grain properties for $\rho_{\rm amb} = 10^{-25}$–$10^{-23}$ g cm^{-3} for each progenitor mass. We employ the model for $\rho_{\rm amb} = 10^{-24}$ g cm^{-3}. Table 2 shows the mass $M_{\rm AC}$ of AC grains produced by faint SNe after the formation/destruction processes. While the fraction of C locked up into AC grains is 4 and 20% for `F13` and `M80`, respectively, it is only 0.04% for `F50`. The ejecta density is larger for `F50` than for the other progenitor masses, and thus C atoms are oxidized to form

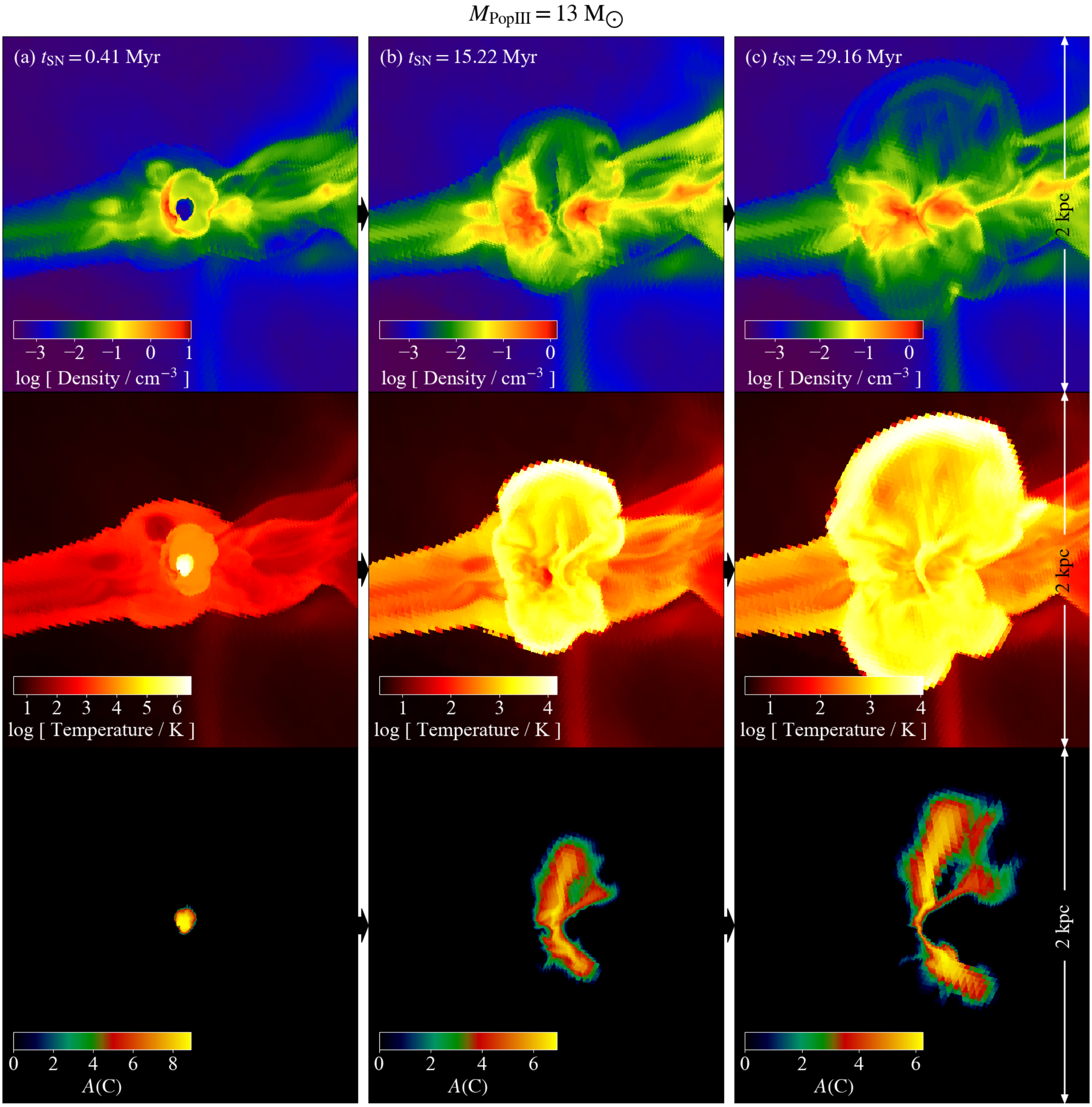

Figure 3. Slice of density, temperature, and C abundance for a progenitor model with a mass $M_{\rm pr} = 13\ {\rm M_\odot}$ at the time $t_{\rm SN} = 0.41$ Myr (column a), 15.22 Myr (column b), and 29.16 Myr (column c) after the SN explosion in a box with a side 2 kpc centered on the centroid of the MH. The axes of the windows are the same as Fig. 1.

CO molecules more rapidly than condensed into AC grains. We can expect that the low abundance of AC prevents the fragmentation of a cloud enriched by the SN. The dashed curves of Fig. 2 show the size distribution of AC grains after the destruction. When grains are sputtered, their size decreases. A tail appears on the smaller end of the initial log-normal size distribution. Following Chiaki et al. (2015, 2017), we also estimate a characteristic grain radius given by $r_{\rm AC,cool} = \langle r^3 \rangle_{\rm AC} / \langle r^2 \rangle_{\rm AC} = 0.012$–$0.096\ \mu$m from the grain properties in our SN models, where $\langle r^n \rangle_{\rm AC} = \int r^n \varphi_{\rm AC}(r) dr$ is the n-th moment of size distribution function $\varphi_{\rm AC}(r)$ at a grain radius r normalized to unity.

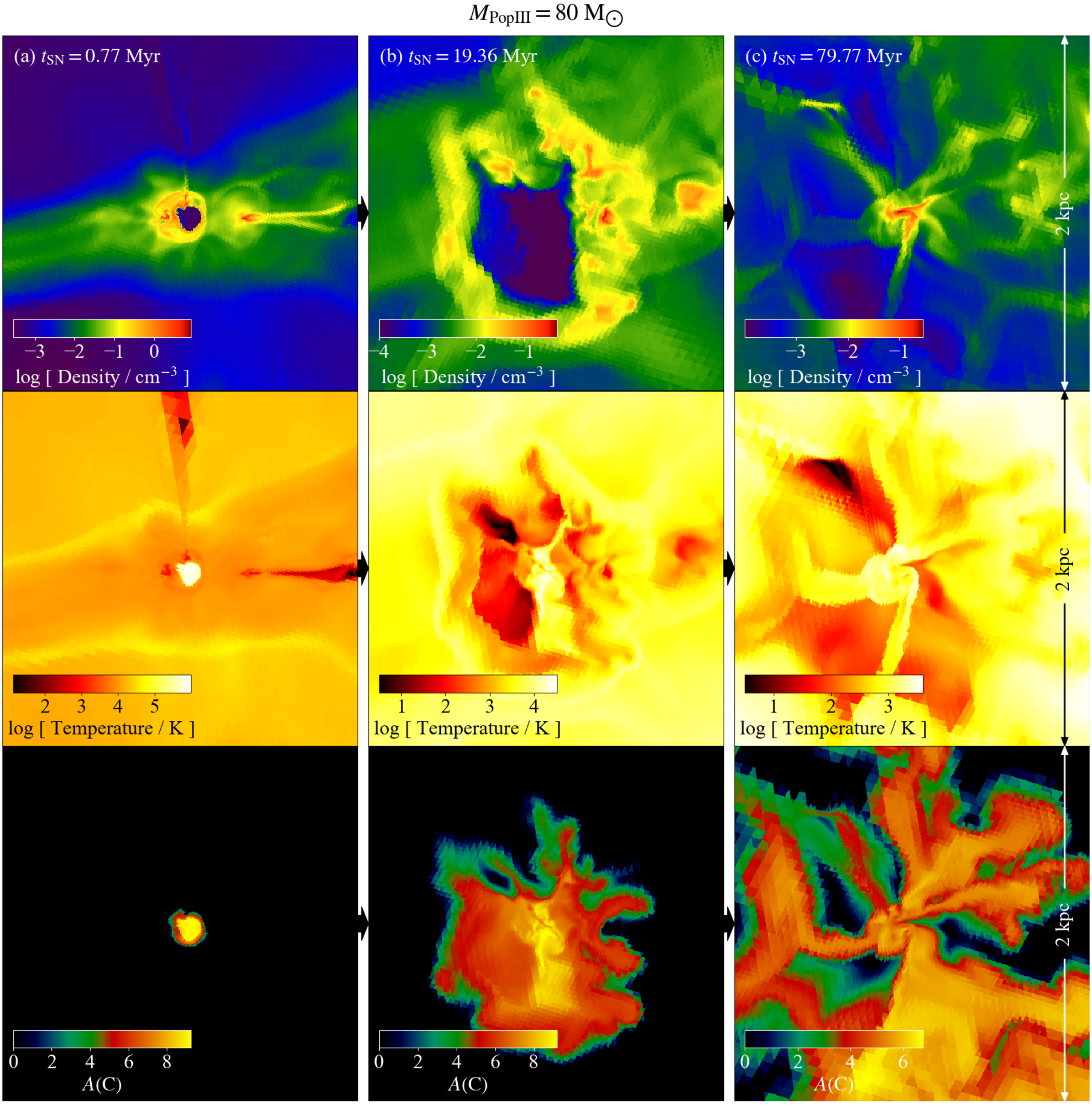

Figure 4. Same as Fig. 3 but for a progenitor mass 80 $M_{\odot}$ at the time $t_{\rm SN}$ = 0.77 Myr (column a), 19.36 Myr (column b), and 79.77 Myr (column c) from the SN explosion.

3 RESULTS

3.1 Enrichment from faint SNe

The evolution of SN shells is affected by the density structure of the H II region created by the ultraviolet (UV) radiation from the progenitor star. The column (a) of Figs. 3 and 4 shows the density, temperature, and carbon abundance, A(C), just after the SN. We do not show the plot for `F50` because it is essentially the same as for `F80`. From these figures, we can see the structure of outer part of H II region which has not been affected by the SN shock. For `F13`, the H II region formed around the Pop III star has a radius $\sim$ 100 pc defined by a D-type shock front. In the region, the density and temperature become $\sim$ 0.01 cm^{-3} and 10^4 K, respectively, and hydrogen atoms are fully ionized. For `F50` and `F80`, the ionization front is decoupled from the D-type shock at a radius $\sim$ 100 pc and reaches $\sim$ kpc beyond the virial radius because of the large ionizing photon emission rates $Q({\rm H}) = 3$–8×10^{49} s^{-1}.

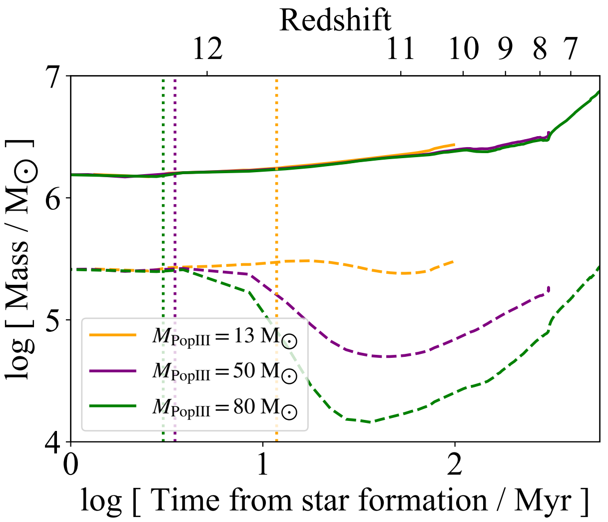

Figure 5. Temporal evolution of DM and baryon mass within the virial radius of the MH (solid and dashed curves, respectively) from the time of Pop III star formation. The vertical dotted lines show the time of SN explosions for progenitor masses 13 $M_\odot$ (orange), 50 $M_\odot$ (purple) and 80 $M_\odot$ (green).

After the SN explosion, a hot bubble ($\sim 10^7$ K) forms around the Pop III remnant. Consistent with analytical blastwave models, the temperature declines adiabatically until the timescale for radiative cooling becomes smaller than the dynamical time of the shell ($\sim$ 0.1–1 Myr). Then, the shell loses its energy through radiative cooling and its expansion is driven by the hot inner bubble in the pressure-driven snowplough (PDS) phase. The inertial force from the decelerated ejecta to the outer swept-up pristine materials drives Rayleigh-Taylor (RT) instabilities and metal mixing between the two regions.

After the inner hot bubble loses its thermal energy, the shell expansion is driven under the conservation of momentum (momentum-conserving snowplough; MCS phase). Figs. 3b and 4b show that the temperature of the inner region begins to decline at a time $t_{\rm SN} = 10$–20 Myr after the SN explosion. The RT fingers develop toward less dense regions in the SN shell. An anti-correlation between density and metal abundance can be seen. Then, the shell collides with dense clumps at distances of $\sim$ 100 pc on the filaments and loses its kinetic energy.

Finally, the clumps return to the MH as shown in Figs. 3c and 4c. The collision of the clumps induces the mixing of the metals which remain in the halo center. For all models, the internal enrichment of the MH occurs and the enriched cloud begins to collapse gravitationally. We estimate the time $t_{\rm ret}$ when the density of the enriched cloud increases up to 10^6 cm^{-3} to be 86.6, 304 and 564 Myr for `F13`, `F50`, and `F80`, respectively (see Table 3). For `F50` and `F80` where the H II region expands beyond the virial radius of the MH, it is expected that the SN shell entirely expands into the void region (Kitayama & Yoshida 2005; Chiaki et al. 2018). We find that the gas infall continues along the cosmic filaments and a part of the shell eventually returns to the MH although it takes longer time than for `F13`. For `F80`, the time $t_{\rm ret} = 564$ Myr corresponds to redshift $z_{\rm ret} = 6.01$. Because we do not consider a UV background, our results are only applicable to volumes that are not ionized by external sources. However, the same sequence can be generalized and is just as likely to occur slightly earlier (i.e., $z \sim 8$) in a different large-scale environment.

Fig. 5 shows the temporal evolution of mass within the virial radius from $t_{\rm form}$ to $t_{\rm ret}$. While the DM mass (solid curves) monotonically increases up to 2.72–$7.47 \times 10^6\ M_\odot$ through the accretion of DM and a halo merger (at $z \sim 8$), the baryon mass (dashed curves) decreases from the time of SN explosions (represented by vertical dotted lines) because the gas is expelled from the MH. At $\sim$ 30 Myr after the explosion, the baryon mass turns to increase up to 3.00–$2.73 \times 10^5\ M_\odot$ because the pristine gas continues to be accreted into the MH. The accretion of pristine gas leads to the dilution of metals.

Fig. 6 shows the distribution of $A({\rm C})$ as a function of distance from the center of the enriched cloud. In the outskirt of the enriched cloud, the metal fraction as well as C abundance shows a large scatter. While the anti-correlation between density and metallicity is still present in some regions, these two quantities are correlated in the other regions where the metal-rich SN shell infalls into the MH (Fig. 4c). The metallicity converges within a radius $\sim$ 0.1 pc (for `F13`) and $\sim$ 10 pc (for `F50` and `F80`) from the cloud center, indicating the minimum length scale of the fluctuation of metallicity. C and Fe abundances in the uniform metallicity region are $([{\rm Fe/H}], A({\rm C})) = (-9.25, 3.80)$, $(-7.94, 5.06)$, and $(-8.28, 4.90)$ for `F13`, `F50`, and `F80`, respectively. The dust-to-gas mass ratio is $\mathcal{D}_{\rm AC} = 1.49 \times 10^{-8}$, 4.11×10^{-10}, and 2.51×10^{-8} (Table 2). The comparison between the dust cooling rate and the gas compressional heating rate suggests that clouds with dust-to-gas mass ratios above $\mathcal{D}_{\rm cr} = 2.6$–$6.3 \times 10^{-9}$ are likely to fragment into low-mass clumps (Schneider et al. 2012a). We now describe the succeeding run-away collapse phase of the enriched clouds, focusing on their thermal evolution and fragmentation properties.

3.2 Recollapse of enriched clouds

In this section, we investigate the chemothermal evolution of the cloud enriched by faint SNe, comparing the results for the three progenitor models. Fig. 7 shows the thermal evolution of the clouds. In the earlier stage of the evolution where the density of cloud center is below $\sim 10^{12}$ cm^{-3}, molecular cooling is dominant. Since metal molecules can contribute to gas cooling for C abundances $A({\rm C}) \gtrsim 5$, in Section 3.2.1, we discuss the thermal evolution in the early collapse stage, focusing on the difference between the two cases with

- lower C abundance ($A({\rm C}) \sim 4$ for `F13`),
- higher C abundance ($A({\rm C}) \sim 5$ for `F50` and `F80`).

In the late collapse stage ($n_{\rm H} \gtrsim 10^{12}$ cm^{-3}), the thermal evolution mainly depends on the amount of AC grains through dust thermal emission cooling. In Section 3.2.2, we compare the two cases with

- lower dust amount ($\mathcal{D}_{\rm AC} \sim 10^{-10}$ for `F50`),
- higher dust amount ($\mathcal{D}_{\rm AC} \sim 10^{-8}$ for `F13` and `F80`).

Table 3. Abundance in the enriched clouds and fragmentation properties

^{1}Run	$^2t_{\rm ret}$ [Myr]	$^3z_{\rm ret}$	$^4M_{\rm halo,dm}$ [M$_\odot$]	$^5M_{\rm halo,b}$ [M$_\odot$]	^{6}[Fe/H]	^7A(C)	$^8\mathcal{D}_{\rm AC}$	$^9r_{\rm AC,cool}$ [μm]	$^{10}N_{\rm frag}$	$^{11}M_{\rm ps}$ [M$_\odot$]	$^{12}R_{\rm ps}$ [au]
`F13`	86.6	10.2	2.72×10^6	3.00×10^5	-9.25	3.80	3.57×10^{-8}	0.119	5	0.0421	1.17
`F50`	304	7.73	3.41×10^6	1.85×10^5	-7.94	5.06	4.52×10^{-10}	0.012	1	0.0294	1.62
`F80`	564	6.01	7.47×10^6	2.73×10^5	-8.28	4.90	2.70×10^{-8}	0.065	1	0.0138	0.868

Note — (1) ID of runs. (2–3) time and redshift when SN shells return to original minihalos. (4–5) dark matter and baryon mass of halos at $t_{\rm ret}$. (6–7) carbon and iron abundance in recollapsing clouds. (8–9) dust-to-gas mass ratio and characteristic grain radius of amorphous carbon (AC) after grain growth. (10) number of fragments. (11–12) mass and radius of the first hydrostatic core.

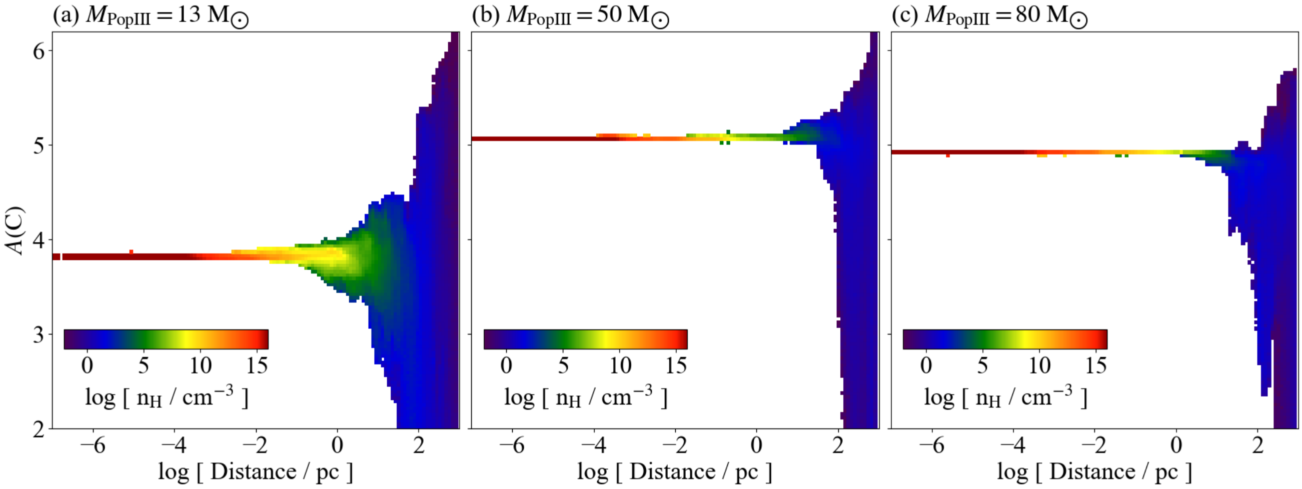

Figure 6. Distribution of C abundance A(C) as a function of distance from the density maximum of the enriched clouds for progenitor masses (a) 13 M$_\odot$, (b) 50 M$_\odot$ and (c) 80 M$_\odot$ at the time when we terminate the simulations.

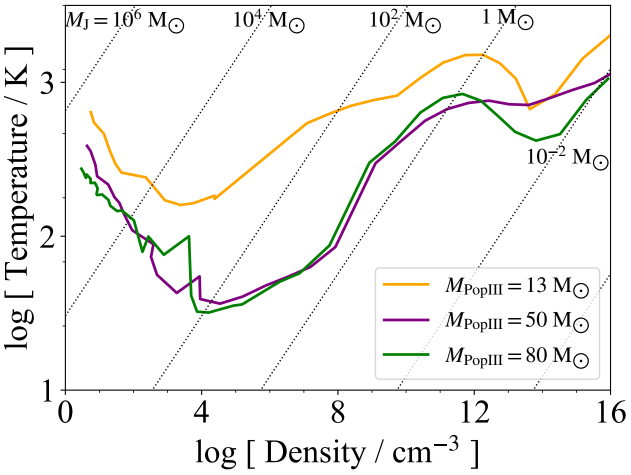

Figure 7. Temporal evolution of temperature of the cloud cores enriched by Pop III SNe with progenitor masses 13 M$_\odot$ (orange), 50 M$_\odot$ (purple) and 80 M$_\odot$ (green). We output snapshots at every time when the highest AMR level is refined and plot the average density and temperature in the region with densities $> n_{\rm H,max}/3$, where $n_{\rm H,max}$ is the maximum density.

3.2.1 Early stage of collapse: $n_{\rm H} \lesssim 10^{12}$ cm^{-3}

Figs. 8 and 9 show the evolution of the abundances of electrons, ions, molecules, and grains and of cooling/heating rates, respectively, as a function of the central density of the cloud core. At densities $n_{\rm H} \sim 1$–10^2 cm^{-3}, hydrogen molecules are the dominant coolant. H$_2$ molecules form mainly through the H$^-$-process:

$$\begin{aligned} {\rm H} + {\rm e}^- &\rightarrow {\rm H}^- + \gamma, \\ {\rm H}^- + {\rm H} &\rightarrow {\rm H}_2 + {\rm e}^-. \end{aligned}$$

The grain surface reaction also contributes to molecular formation. The H$_2$ fraction relative to hydrogen nuclei becomes $\sim 10^{-3}$ for all models. When the temperature drops below 150 K, HD molecules form through the reactions

$$\begin{aligned} {\rm H}_2 + {\rm D} &\rightarrow {\rm HD} + {\rm H}, \\ {\rm H}_2 + {\rm D}^+ &\rightarrow {\rm HD} + {\rm H}^+. \end{aligned}$$

HD cooling becomes dominant at $n_{\rm H} \sim 10^2$–10^4 cm^{-3}. Columns (a) of Figs. 10 and 11 show the morphology of the cloud core for `F13` and `F80` models, respectively.We do not show the plot for `F50` because the cloud morphology is similar to that for `F80` in the early collapse stage. For all models HD cooling leads to a bar-mode instability on a spherically symmetric core (Lai 2000; Hanawa & Matsumoto 2000). This cloud deformation is the precursor of fragmentation (Tsuribe & Omukai 2006). However, low-mass stars

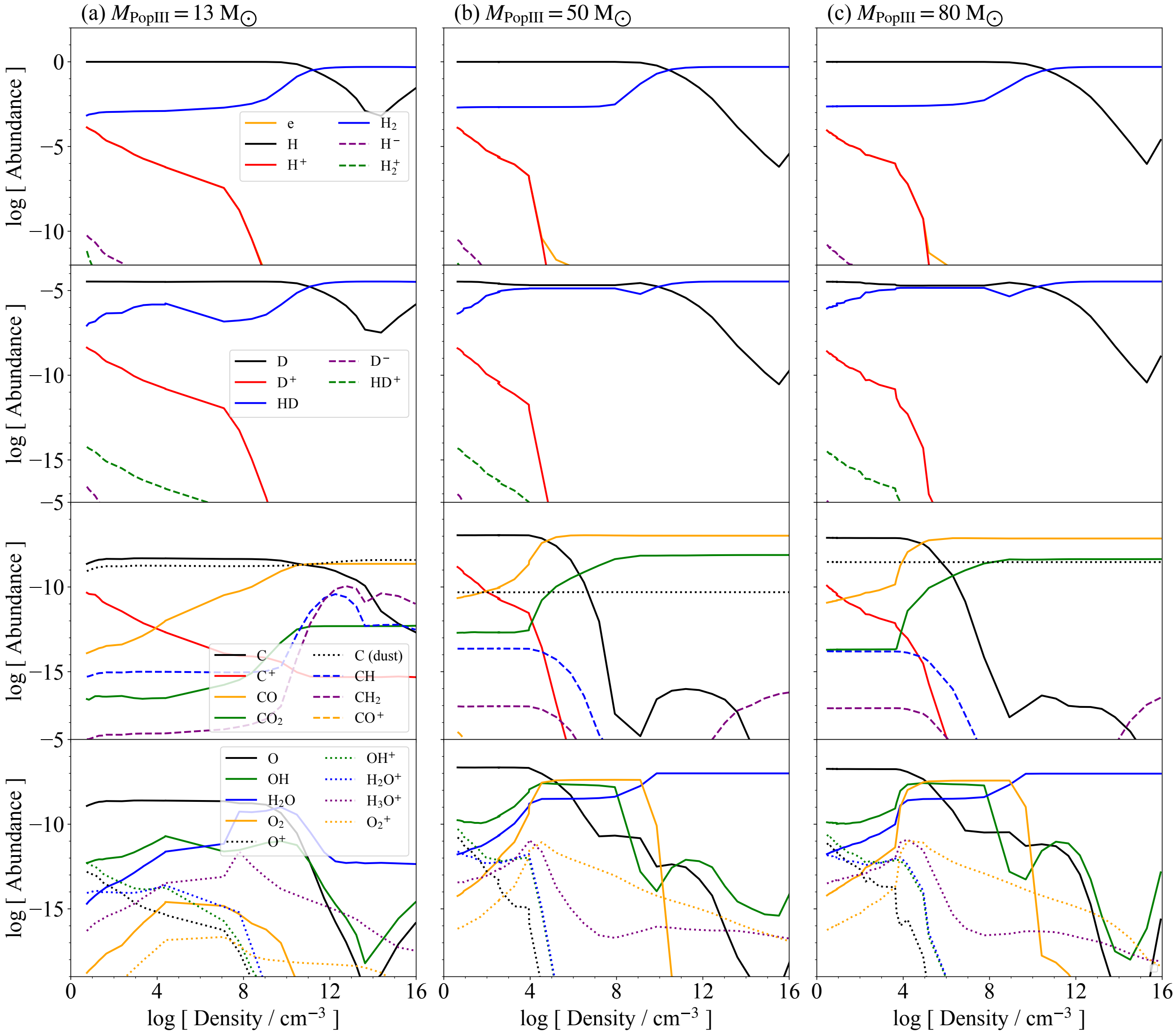

Figure 8. Evolution of the abundance of electrons, atoms, ions, molecules, and grains in the cloud cores enriched by the Pop III SNe with progenitor masses 13 $M_{\odot}$ (column a), 50 $M_{\odot}$ (column b) and 80 $M_{\odot}$ (column c) as a function of density of the cloud cores.

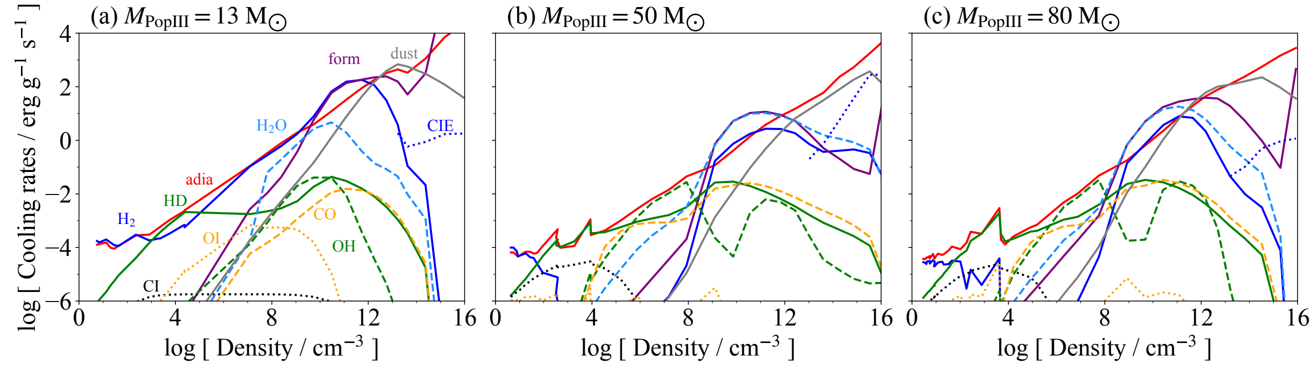

Figure 9. Evolution of cooling and heating rates of the cloud cores enriched by Pop III SNe with progenitor masses (a) 13 $M_{\odot}$, (b) 50 $M_{\odot}$ and (c) 80 $M_{\odot}$ as a function of core density. We plot the heating rates of adiabatic gas compression ("adia"; red solid) and H_2 formation ("form"; purple solid) and radiative cooling rates of H_2 (blue solid), HD (green solid), C I (black dotted), O I (orange dotted), CO (orange dashed), OH (green dashed), H_2O (cyan dashed), dust (grey solid), and CIE (blue dotted).

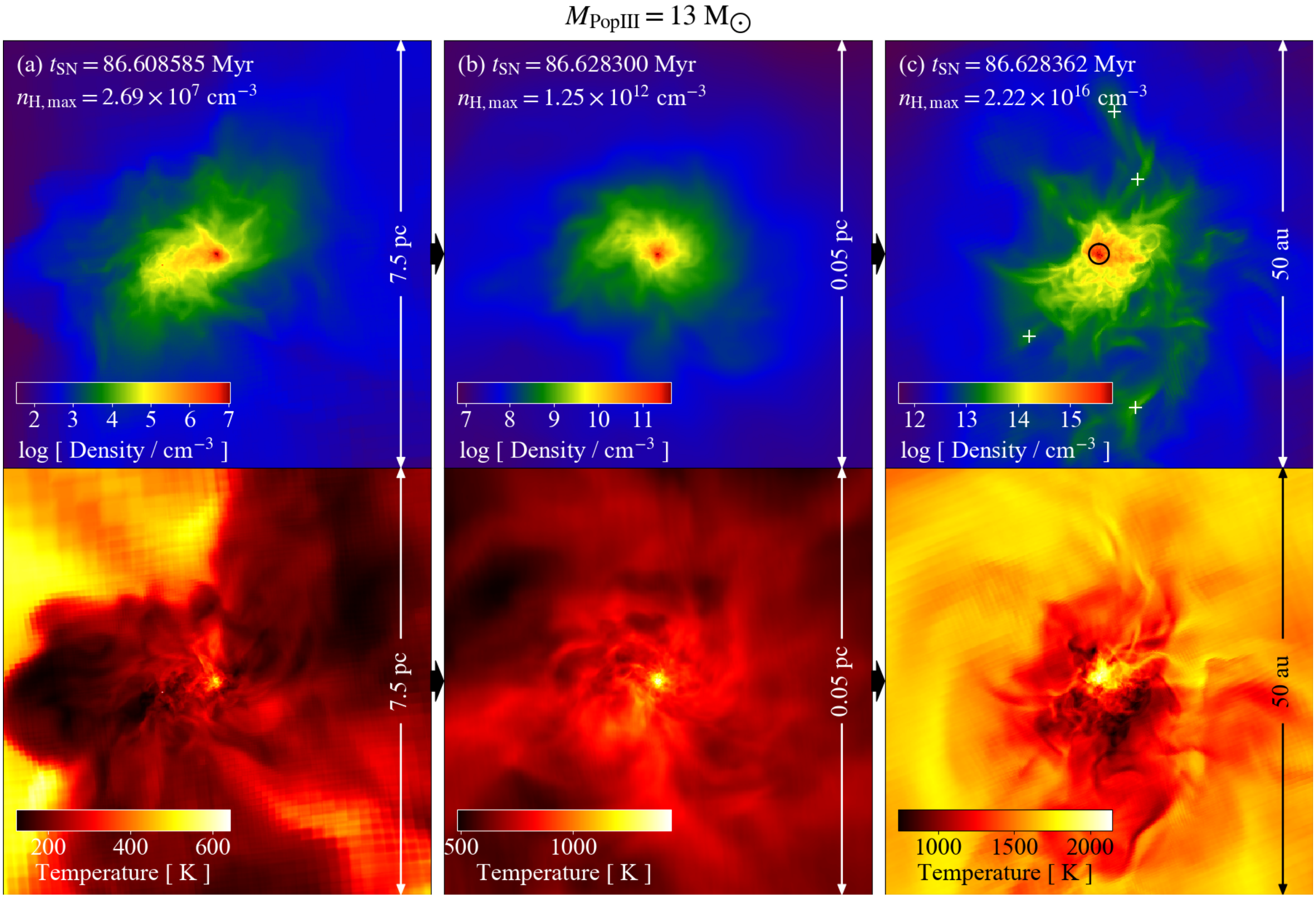

Figure 10. Density-weighted projection of density and temperature in a box centered on the density maximum of the enriched clouds for a progenitor mass 13 $M_\odot$. We plot the snapshots at the time when the maximum density $n_{\rm H,max}$ reaches $\sim 10^7$ cm^{-3} (column a), 10^{12} cm^{-3} (column b), and 10^{16} cm^{-3} (column c). The circle and plus symbols are plotted on the density maxima of a hydrostatic core and clumps forming through fragmentation induced by dust thermal emission cooling, respectively. The x and z axes of the windows are respectively parallel to the major and minor axes of the momentum of inertia of the region with densities $> n_{\rm H,max}/3$.

which can survive until the present day are unlikely to form through molecular cooling because the corresponding Jeans mass is still relatively large ($M_{\rm J} \sim 10^2$–10^4 $M_\odot$) as indicated by the black dotted lines in Fig. 7.

At densities $n_{\rm H} \sim 10^4$–10^8 cm^{-3}, the temperature is smaller (30 K) for `F50` and `F80` than for `F13` (150 K) because OH cooling becomes dominant in the former case. OH and O_2 molecules form mainly through the reactions

$$\rm O + H \rightarrow OH + \gamma .$$

at a density $\sim 10^4$ cm^{-3}. For `F13`, OH cooling is less efficient because the O abundance ([O/H] = −5.33) is smaller than for the other models ([O/H] = −3.34 and −3.44 for `F50` and `F80`, respectively). Further, O is rapidly depleted into CO molecules because C has a larger abundance with respect over O ([C/O] = +0.691) compared to the other models ([C/O] = −0.0269 and −0.0855 for `F50` and `F80`).

At densities $n_{\rm H} \sim 10^8$–10^{12} cm^{-3}, the temperature increases rapidly due to gas heating along with H_2 formation through three-body reactions

$$\begin{aligned} \rm H + H + H &\rightarrow \rm H_2 + H, \\ \rm H + H + H_2 &\rightarrow \rm H_2 + H_2 . \end{aligned}$$

The temperature increase is more significant in models `F50` and `F80` than in model `F13` because the temperature just before H_2 formation heating becomes dominant is smaller ($\sim$ 100 K) owing to cooling from OH as well as H_2O molecules forming through the reaction

$$\rm OH + H_2 \rightarrow H_2O + H .$$

This rapid gas heating stabilizes the cloud against the deformation of the cloud core. A hot spherical hydrostatic core defined by accretion shocks forms at a radius $\sim 10^{-2}$ pc for `F80` (Fig. 11b). Whereas, density fluctuations remain within this radius scale through the moderate gas heating for `F13` (Fig. 10b). Fig. 12 shows the radial profile of density, temperature, and radial velocity. The velocity increases inward by $\sim$ 1 km s^{-1} at a radius $\sim 10^{-2}$ pc where temperature rapidly increases for `F50` and `F80` while the velocity smoothly decreases for `F13`.

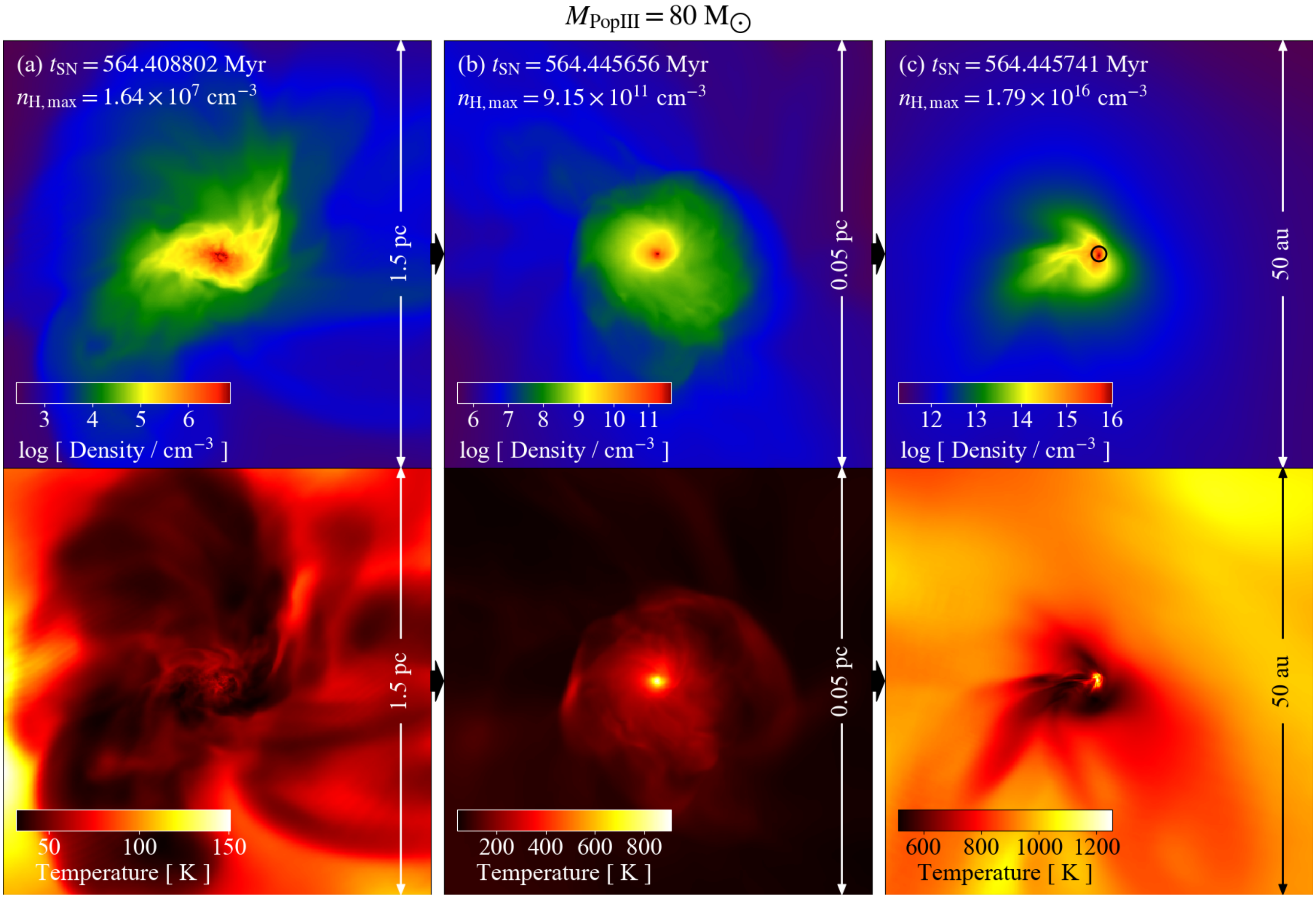

Figure 11. Same as Fig. 10 but for a progenitor mass 80 M$_\odot$. In this run, fragmentation does not occur and thus only a hydrostatic core is shown by the circle.

3.2.2 Late stage of collapse: $n_{\rm H} \gtrsim 10^{12}$ cm^{-3}

For `F13`, AC grains grow in size through accretion of gas phase C atoms. Fig. 2 shows the size distribution of AC grains before (dashed curves) and after (solid curves) grain growth. The size distribution shifts toward the larger radii by $\Delta r = 0.02$ μm. Fig. 8a shows that the abundance of C atoms locked up into AC grains (black dotted curve) slightly increases at a density $n_{\rm H} \sim 10^{13}$ cm^{-3}. The dust-to-gas mass ratio increases from 1.49×10^{-8} to 3.57×10^{-8} (Tables 2 and 3) and the grain cooling rate is enhanced. For the other models, grain growth is not effective because C atoms are mostly oxidized into CO molecules at densities $n_{\rm H} \sim 10^5$ cm^{-3} due to the larger O/C abundance ratio.

At densities $n_{\rm H} = 10^{12}$–10^{14} cm^{-3}, while the temperature evolves nearly isothermally for the model with low dust content (`F50`), the temperature decreases due to cooling by dust thermal emission for the models with high dust content (`F13` and `F80`). The condition where the dust cooling rate exceeds the adiabatic compressional heating (the main heating source of the clouds) at a given density $n_{\rm H}$ and temperature T is

$$\frac{\mathcal{D}_{\rm AC}}{r_{\rm AC,cool}} > 1.86 \times 10^{-7}\ \mu{\rm m}^{-1} \left(\frac{T}{500\ {\rm K}}\right)^{-1/2} \times \left(\frac{n_{\rm H}}{10^{13}\ {\rm cm}^{-3}}\right)^{-1/2} . \qquad (1)$$

(Schneider et al. 2012a; Chiaki et al. 2015). Assuming the values $\mathcal{D}_{\rm AC}$ and $r_{\rm AC,cool}$ achieved after grain growth (Table 3), we find that, for models `F13` and `F80`, $\mathcal{D}_{\rm AC}$ / $r_{\rm AC,cool} = 3.00 \times 10^{-7}$ μm^{-1} and 4.15×10^{-7} μm^{-1}, respectively, above the critical value while, for `F50` 3.77×10^{-8} μm^{-1}, below the critical value.

Finally, in the region with densities $> 10^{13}$ cm^{-3}, since the grains become thermally coupled with the gas, the temperature starts to increase again. Then, the gas becomes optically thick to continuum radiation. The cloud core evolves nearly adiabatically and a hydrostatic core, which can not contract further, forms as we can see at a radius ~ 1 au ($\sim 10^{-6}$ pc) in Fig. 12 (Larson 1969; Penston 1969).

3.3 Fragmentation of enriched clouds

Whether fragmentation occurs in the later stage of collapse or not depends on the different thermal evolution among the three progenitor models. For `F50`, cloud fragmentation does

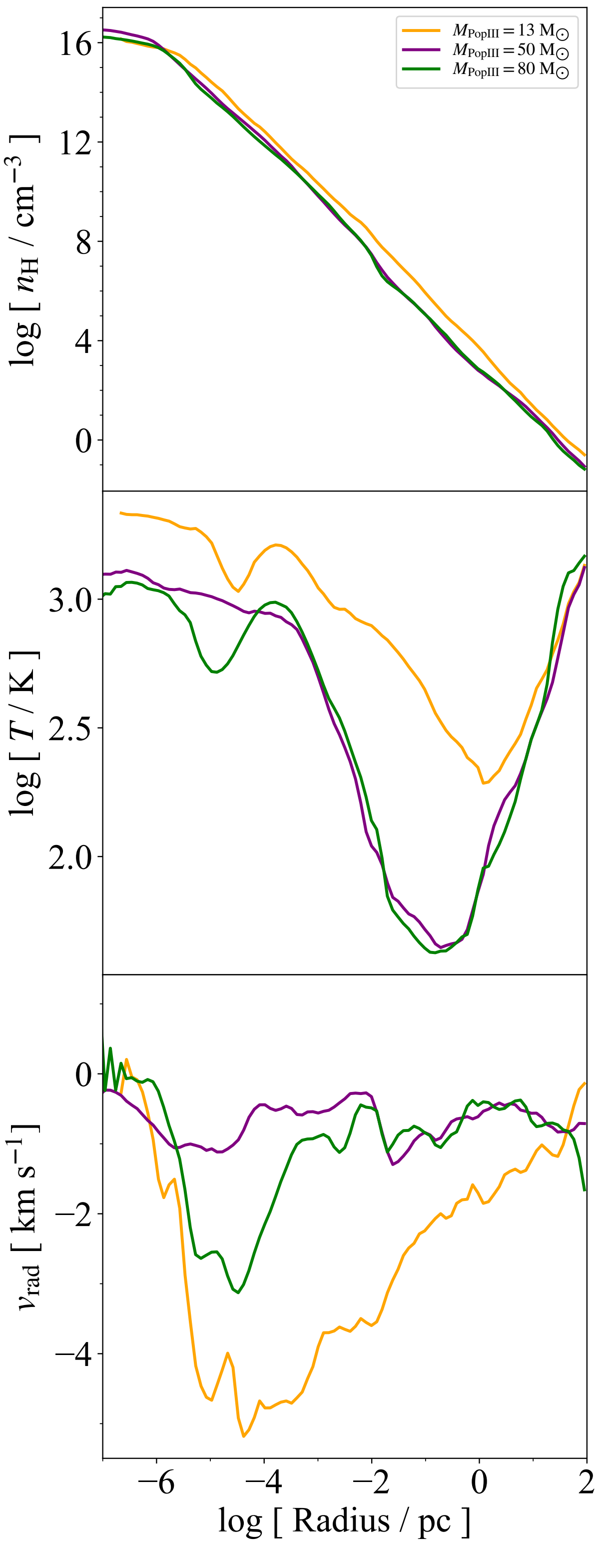

Figure 12. Radial profile of density, temperature, and radial velocity at the time when we terminate our simulations for progenitor masses 13 M$_\odot$ (orange), 50 M$_\odot$ (purple) and 80 M$_\odot$ (green).

not occur because of inefficient dust cooling (Eq. 1). Fig. 13 shows the snapshot of the cloud core in the later collapse stage for `F50`. A disk structure forms around a central hydrostatic core (circle) as for primordial clouds (Clark et al. 2011; Greif et al. 2012; Hirano & Bromm 2017) because the temperature evolution in the later stage is similar to the primordial clouds as H_2 cooling is dominant (Fig. 9b). In Fig. 13, we show the disk from the face-on and edge-on views. The disk is gravitationally unstable and dense spiral arms form. The arms might fragment in the further evolution of the accretion disk as we discuss in Section 4.

For higher dust content, although dust cooling becomes effective in both runs, the cloud core fragments into isolated filamentary structures for `F13` (Fig. 10c) while fragmentation does not occur for `F80` (Fig. 11c). In the latter case, only short filaments connected with the central core appear. For the filaments to fragment, their aspect ratio should grow up to 20–30 (Tsuribe & Omukai 2006; Chiaki et al. 2016). In this model, rapid gas heating along with H_2 molecular formation has made the cloud stable against the deformation at densities $n_{\rm H} = 10^8$–10^{12} cm^{-3} before dust cooling occurs. Therefore, the timescale for deformation of the spherical cloud core to sufficiently thin filaments is longer than the dynamical timescale of the cloud while the opposite is true for `F13` model. As seen in Section 3.2.1, this difference of heating rate is due to the different cooling efficiency of metal molecules (OH/H_2O) before the onset of H_2 formation heating.

Our detailed chemistry/cooling model shows that the fragmentation properties of the clouds enriched by faint SNe depend on multiple cooling/heating processes (1) dust thermal emission cooling, (2) H_2 formation heating, and (3) OH/H_2O molecular cooling (see also Chiaki et al. 2016).

More quantitatively, we count the number and mass of clumps within 100 au from the maximum density with a clump-finding algorithm. This identifies isolated clumps by using iso-density contours (Smith et al. 2009; Turk et al. 2011). If a candidate clump does not meet the user-defined validators, it is merged with another clump or discarded. In this work, we impose the following three criteria:

(i) the minimum number of cells in a clump is 20,
(ii) the minimum density of the cell in a clump is $n_{\rm H,th} = 10^{13}$ cm^{-3},
(iii) the minimum mass of a clump is $M_{\rm th} = 10^{-3}$ M$_\odot$ (~ 1 Jupiter mass).

In the criteria (ii), we choose the threshold density $n_{\rm H,th} = 10^{13}$ cm^{-3}, where dust cooling becomes dominant, to select clumps formed through dust-induced fragmentation. Here we do not require the clumps to be gravitationally bound. For the most massive clump, which has developed a hydrostatic core, we estimate the mass $M_{\rm ps}$ and radius $R_{\rm ps}$ above which the gravitational energy $3GM_{\rm ps}^2/5R_{\rm ps}$ exceeds the total thermal energy. We hereafter call the primary clump as "protostar". Since the computational time is set by the short dynamical time of the dense protostar, when we terminate the simulation the secondary clumps are still in the early phase of their gravitational growth. Therefore, in this work we just show their mass derived from the clump-finding algorithm. We hereafter call the secondary clumps as just "clumps".

For `F13`, the number $N_{\rm frag}$ of identified clumps is five

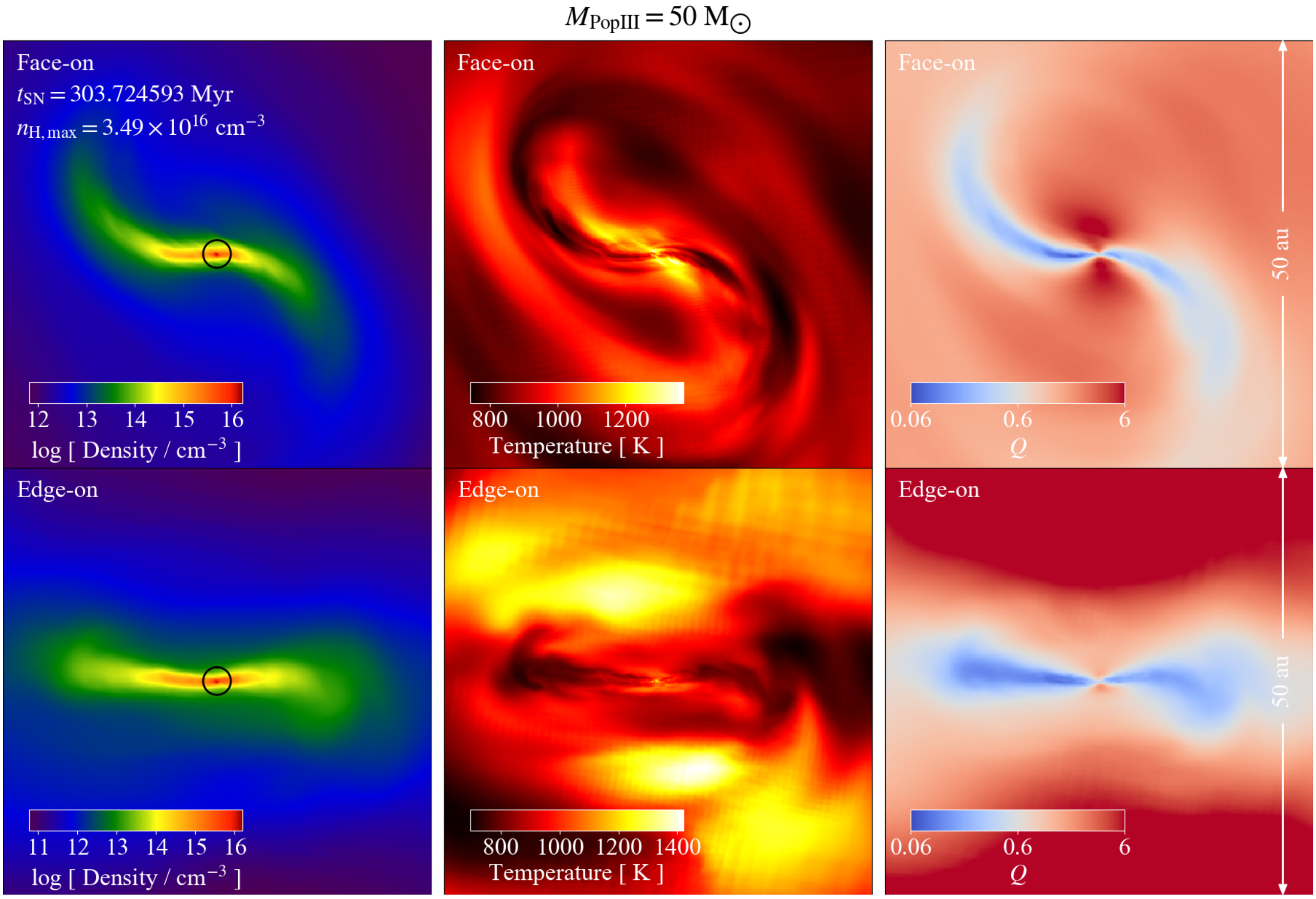

Figure 13. *Left to right*: density-weighted projection of density, temperature, and the Toomre Q parameter (see Section 4.2.3) in a box with a side 50 au centered on the density maximum of the enriched clouds for a progenitor masses 50 M$_\odot$. The top and bottom panels of each column show the disk from the face-on and edge-on view, respectively. The circle denotes the radius of a hydrostatic core forming in the central optically thick region.

(Table 3). The circle and plus symbols in Fig. 10c depict the distribution of the primary protostar and the secondary clumps, respectively. The mass and radius of the protostar are $(M_{\rm ps}, R_{\rm ps}) = (0.0421$ M$_\odot$, 1.17 au). The masses of the four clumps are 1.06×10^{-2}, 2.35×10^{-3}, 1.55×10^{-3}, and 1.21×10^{-3} M$_\odot$. The separation of clumps ($\sim$ 10 au) and mass of the protostar are comparable to the local Jeans length and mass for $n_{\rm H} = 10^{14}$ cm^{-3} and $T = 1000$ K, which indicates that the fragmentation is induced by dust cooling. For `F50` and `F80`, the clump-finding algorithm can not identify any secondary clumps ($N_{\rm frag} = 1$). The mass and radius of the protostar are (0.0294 M$_\odot$, 1.62 au) and (0.0138 M$_\odot$, 0.868 au) for `F50` and `F80`, respectively.

Although these protostars and clumps will gain mass by accreting the ambient gas in the subsequent evolution until they reach the main-sequence as discussed in Section 4, dust-induced low-mass fragments can form in model `F13`.

4 DISCUSSION

4.1 Prediction of observations

We have so far presented the results of our simulation of metal enrichment from faint SNe and the fragmentation properties of the enriched clouds. If the protostars in the clouds grow to low-mass stars and the MH is accreted into the Milky Way halo or Local Group dwarf galaxies through DM halo mergers, they can be observed as EMP stars. In this section, we discuss their observability. The colored symbols in Fig. 14 depict the distribution of elemental abundances of the enriched clouds on the A(C)-[Fe/H] diagram used in Yoon et al. (2016). We also plot the abundances of protostars forming in the cloud enriched from a normal CCSN with a $M_{\rm PopIII} = 13$ M$_\odot$ (black square) in the simulation of our previous study (Paper I), hereafter called the run `C13`. The filled and open symbols indicate the runs where fragmentation occurs and not, respectively.

For comparison, we plot the abundances of observed EMP stars from the SAGA database (Suda et al. 2008). The blue dots represent the C-normal stars with [C/Fe] $<$ 0.7 or stars whose C abundances are not constrained. The other colors represent C-enhanced stars with [C/Fe] $>$ 0.7,

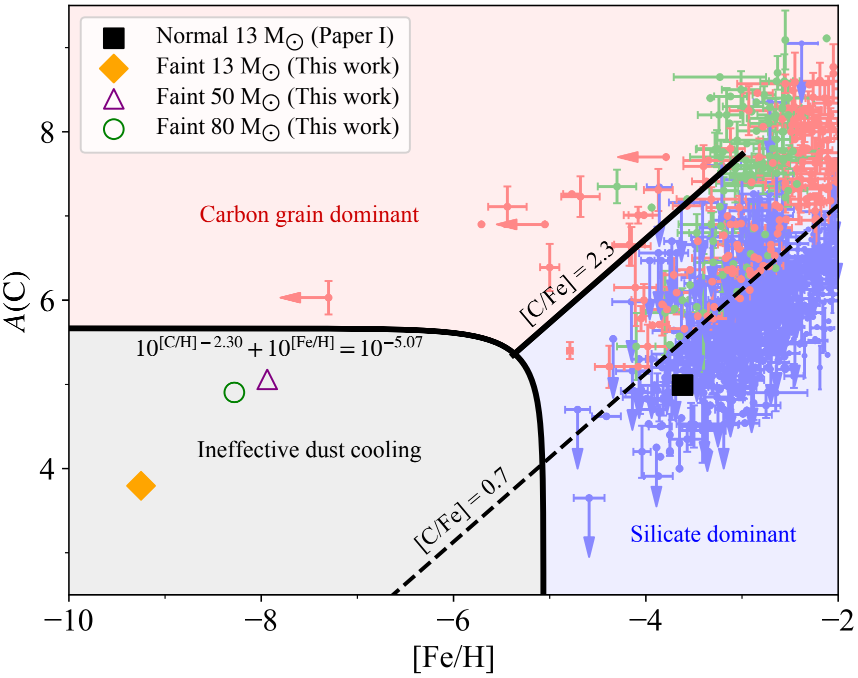

Figure 14. Elemental abundances of clouds enriched by faint SNe for progenitor masses $M_{\rm PopIII} = 13\ {\rm M}_\odot$ (orange diamond), 50 M$_\odot$ (purple triangle), and 80 M$_\odot$ (green circle) on the A(C)-[Fe/H] plane. The black square shows the C and Fe abundances of the clouds enriched by a normal CCSN with a $M_{\rm PopIII} = 13\ {\rm M}_\odot$ from our previous simulation (Paper I). The filled and open symbols indicate the runs where cloud fragmentation occurs or not, respectively. The dots show the abundances of observed stars retrieved from the SAGA database (Suda et al. 2008): *blue dots* C-normal stars ([C/Fe] < 0.7) or stars whose C abundances are not constrained, *green dots* CEMP-s stars ([C/Fe] > 0.7 and [Ba/Fe] > 0.5), and *red dots* CEMP-no stars ([C/Fe] > 0.7 and [Ba/Fe] < 0.5) or CEMP stars whose Ba abundances are not constrained. We also plot the criterion for CEMP stars ([C/Fe] $= 0.7$; Aoki et al. 2007). The black solid line shows the critical condition defining the carbon grain dominant region (red shaded) and silicate dominant region (blue shaded). In the grey shaded region below the black solid curve, no stars have been identified, which may suggest that dust cooling is ineffective in their parent clouds and low-mass stars hardly form (C17).

following the definition of Aoki et al. (2007). The green and grey dots represent CEMP-s with [Ba/Fe] > 0.5 and CEMP-no with [Ba/Fe] < 0.5 or stars whose Ba abundances are not constrained, respectively. As C17 found, no stars have been observed in the grey shaded area bounded by the black solid curve.

From a comparison of our simulation results with the observational data, we can see that the abundances for `C13` ([Fe/H], A(C)) $= (-3.62, 4.99)$ are in the range of observed C-normal stars ([Fe/H] > -5) and can explain the formation of C-normal stars. Whereas, the abundances for `F13`, `F50`, and `F80` ([Fe/H] $= [-9.25 : -7.94]$ and A(C) $= [3.80 : 5.06]$) are below the range of observed CEMP Group III stars (A(C) $\gtrsim 6$) although the abundance ratio [C/Fe] $= 4.57$–4.75 is consistent with the observed values.

We now discuss the reason why the elemental abundances for the faint SN models are systematically smaller than those for the normal CCSN model. The elemental abundances of recollapsing clouds depend on the following three parameters (Ritter et al. 2015, Paper I). First, the mass of an element M ejected from SNe, $M_{\rm M}$, is an important value. Second, the fraction $f_{\rm ret}$ of metals that return to the MH determines the elemental abundances of the enriched clouds. We can estimate this as the fraction of solid angles where metal dispersion is interrupted on the contact surfaces between the SN shell and cosmic filaments or interstellar gas clumps. Finally, the dilution efficiency of the metals is important, i.e., the mass of pristine gas with which the metals are mixed. The simplest estimate is to use the pristine gas mass within the virial radius, similar to semi-analytic works (e.g., de Bennassuti et al. 2017; Hartwig et al. 2018). Since the distribution of elements is not uniform within the virial radius of the MH, we consider only the dense central cloud where the elemental abundances are uniform (Fig. 6). In this work, we define the pristine gas mass as the Jeans mass $M_{\rm cloud}$, at the density $10^3\ {\rm cm}^{-3}$ (see the black dotted lines in Fig. 7). With these three parameters ($M_{\rm M}$, $f_{\rm ret}$, and $M_{\rm cloud}$), we can estimate C and Fe abundances in the enriched cloud to be

$$A({\rm C}) = 12 + \log\left(\frac{f_{\rm ret} M_{\rm C}/\mu_{\rm C}}{X_{\rm H} M_{\rm cloud}}\right), \quad (2)$$

$$[{\rm Fe/H}] = 12 + \log\left(\frac{f_{\rm ret} M_{\rm Fe}/\mu_{\rm Fe}}{X_{\rm H} M_{\rm cloud}}\right) - A_\odot({\rm Fe}), \quad (3)$$

where $\mu_{\rm C} = 12$ and $\mu_{\rm Fe} = 56$ are the molecular masses of C and Fe, respectively.

For `C13`, the ejected mass of C and Fe is ($M_{\rm C}$, $M_{\rm Fe}$) $=$ (0.5 M$_\odot$, 0.2 M$_\odot$). The metal dispersion is interrupted by a clump with a distance $D_{\rm cl} = 50$ pc and radius $R_{\rm cl} = 6$ pc. Therefore, $f_{\rm ret} = \pi R_{\rm cl}^2/4\pi D_{\rm cl}^2 \sim 0.004$. With a cloud mass $M_{\rm cloud} = 2000\ {\rm M}_\odot$, we can estimate the abundances as ([Fe/H], A(C)) $= (-3.6, 5.0)$, consistent with the simulation result.[7] Even with the small $f_{\rm ret}$, we can explain the formation of C-normal EMP stars. For `F13`, the mass of ejected metals are $(M_{\rm C}, M_{\rm Fe}) = (0.08~{\rm M_{\odot}}, 10^{-6}~{\rm M_{\odot}})$. Since the density structure of ISM is similar to that for `C13`, the return fraction is $f_{\rm ret} \sim 0.004$. With the cloud mass $M_{\rm cloud} = 4000~{\rm M_{\odot}}$, ([Fe/H], A(C)) = (−9.2, 3.9). Compared to `C13`, the ejected C mass is smaller by a factor of six. Also, the cloud mass is larger because the gas temperature is higher due to the smaller metallicity. Consequently, the solid angle where metal dispersion is interrupted becomes smaller.

For `F50` and `F80`, the metal yield is $(M_{\rm C}, M_{\rm Fe}) = (1~{\rm M_{\odot}}, 10^{-5}~{\rm M_{\odot}})$. The radius of the interacting region of the shell with the ambient clump is larger $D_{\rm cl} = 100$ pc than for `F13` because filaments and clumps within $R_{\rm cl}$ are photoevapolated by the strong UV emission. It takes longer time until the SN shells return and the clump has gravitationally grown to $R_{\rm cl} = 7$ pc. With $f_{\rm ret} = \pi R_{\rm cl}^2 / 4\pi D_{\rm cl} \sim 0.001$ and $M_{\rm cloud} = 1000~{\rm M_{\odot}}$, ([Fe/H], A(C)) = (−8.0, 5.1), which is consistent with our simulation results. Compared to `C13`, the ejected C mass is larger by a factor of three. However, $f_{\rm ret}$ is smaller by a factor of three because the radius of the region within which metals are mixed is larger with larger explosion energies ($E_{\rm SN} = 2.6$–5.2×10^{51} erg). Consequently, A(C) in the enriched clouds becomes comparable to that for `C13`. The value is smaller than A(C) of the observed CEMP Group III stars.

For the MH and Pop III faint SNe investigated here, the enrichment from a single faint SNe can hardly explain the formation of CEMP stars with the observed metallicity range. We discuss their formation paths in general cases in Section 4.2.1.

We also find that cloud fragmentation occurs through dust cooling for `F13` even with the lowest metallicity ([Fe/H] ~ -9). This is because the condensation efficiency of C into AC grains is large ($f_{\rm AC,C} = 0.262$) and the cloud avoids rapid H_2 formation heating (Section 3.2.1). This indicates that low-mass stars with a metallicity [Fe/H] ~ -9 can form but the abundance is below the region where CEMP stars have been observed so far (grey shaded region in Fig. 14).

C17 estimated the effective grain radius of AC to be $r_{\rm AC,cool}/f_{\rm AC,C} \sim 10~\mu$m at which the dust cooling rate overcomes the compressional heating rate (Eq. 1) above the critical C abundance $A_{\rm cr}({\rm C}) \sim 6$. The dust model of M14 used in this work suggests the formation of smaller grains with $r_{\rm AC,cool}/f_{\rm AC,C} = 0.454~\mu$m for `F13` in faint SNe. Grains smaller than 10 μm can induce cloud fragmentation for C abundances lower than $A_{\rm cr}({\rm C}) \sim 6$.

A semi-analytic study of galactic chemical evolution including the contributions from faint SNe (Komiya et al. 2020) gives a consistent result with our simulations. They point out that faint SNe might overproduce stars with significantly small metallicities ([Fe/H] < -7) compared to the metallicity distribution function (MDF) of observed stars because these SNe produce smaller mass of metals than normal CCSNe (see also de Bennassuti et al. 2014, 2017). Unfortunately, the MDF in the low metallicity end still has a large uncertainty because the number of observed stars with [Fe/H] < -4.5 is small (~ 10). Future surveys and spectroscopic studies with Subaru/PFS (Takada et al. 2014) and the Thirty-Meter Telescope (TMT) (Skidmore et al. 2015) will probe the chemical enrichment process in the early Universe.

4.2 Caveats

4.2.1 *General initial conditions*

In this work, we have investigated the metal enrichment from faint SNe with progenitor masses $M_{\rm PopIII} = 13$, 50, and 80 ${\rm M_{\odot}}$ in a MH with a $M_{\rm halo} = 2.1 \times 10^6~{\rm M_{\odot}}$. The MH is relatively high-mass, compared to the mass range of MHs derived from large-volume cosmological simulations, 2×10^5–$3 \times 10^6~{\rm M_{\odot}}$ (Susa et al. 2014; Hirano et al. 2014, 2015). Chiaki et al. (2018) investigated CEMP star formation for different initial conditions with $M_{\rm halo} = 3 \times 10^5$–$3 \times 10^6~{\rm M_{\odot}}$ and $M_{\rm PopIII} = 20$–$30~{\rm M_{\odot}}$, and found that the elemental abundances in recollapsing clouds are larger for lower-mass MHs. For a high-mass MH ($3 \times 10^6~{\rm M_{\odot}}$), the SN shell becomes gravitationally unstable during its expansion because the H II region does not expand outside the virial radius, and the shell rapidly loses its thermal energy once it encounters the neutral medium. The SN shell enriches a nearby cloud and collapses away from the explosion site, offset from the halo center. A smaller fraction of metals mixes into the cloud that has already begun to collapse. Consequently, the elemental abundances are smaller than the low-mass case ($3 \times 10^5~{\rm M_{\odot}}$), where the explosion disrupts the MH and recollapses into the halo center. For low-mass MHs, the iron abundance can be estimated to be in the range [Fe/H] = [−8.63 : −4.34], and thus the formation of CEMP stars can be explained by the enrichment from a single faint SN in several cases. In Chiaki et al. (2018), the resolution was limited (~ 1 pc) compared to this work, and the formation of dust grains was not considered. We will investigate CEMP star formation for a wide range of MH and Pop III stellar masses with a resolution similar to the present study in large cosmological simulations in future works.

4.2.2 *Multiple source of metals*

In this work, we restrict our focus on Pop III star formation in a single MH. There are several MHs around the central MH within 1 kpc (Fig. 1) and they might contribute to their mutual enrichment (Smith et al. 2015). For `F80`, it takes 500 Myr until the metals from the central MH return and during this time interval the metals ejected by other MHs may possibly enrich the MH. The effect of multi-enrichment will be to create a superposition of elemental abundances having multiple SN progenitors (Salvadori et al. 2007, 2010; de Bennassuti et al. 2015, 2017; Hartwig et al. 2018). However, in this work we consider the formation of a single Pop III star in the MH. Numerical simulations of primordial clouds suggest that the stellar cluster formation through disk fragmentation may occur (Turk et al. 2009; Clark et al. 2011; Greif et al. 2012). A cosmological simulation has also indicated that multiple Pop III stars form in each MH (Skinner & Wise 2020). In the case of multiple SNe in a MH, Ritter

---

[7] Compared to the estimation in Paper I, we improve the approximation accuracy, and thus the estimation is slightly changed.

et al. (2015) found that the gas in the MH is evacuated by the first SN blast wave but a non-negligible fraction (~ 0.3) of metals ejected from the secondary SNe contribute to the enrichment of the MH.

In galactic archaeology, the number of progenitors of EMP stars is important value as the mass and explosion energy of the Pop III stars can be directly traced back from the elemental abundances of singly enriched stars (Ishigaki et al. 2018; Hartwig et al. 2018; Choplin, Tominaga & Ishigaki 2019). In their semi-analytic studies, de Bennassuti et al. (2017) predict that stars with metallicities $[\mathrm{Fe/H}] \lesssim -5$ can be the very second generation of stars, which is the metallicity range that we have investigated. In order to study the formation of stars with larger metallicities, we will investigate multiple star formation in each MH and mutual metal enrichment between close MHs in cosmological simulations to see the frequency of multi-enrichment in forthcoming papers.

4.2.3 Growth of protostars

When we terminate the simulations, protostars have formed in the optically thick region. Their mass is $\sim 0.01\ \mathrm{M}_{\odot}$, comparable to the Jeans mass with density $\sim 10^{14}\ \mathrm{cm}^{-3}$ and temperature ~ 1000 K. We should note that, until the protostars reach the zero-age main-sequence, their masses grow through the accretion of the ambient materials (Hosokawa et al. 2011; Hirano et al. 2014). For `F13`, if the protostars remain low-mass, with a mass less than $0.8\ \mathrm{M}_{\odot}$ despite competitive accretion among the fragments, the stars will be observed in the present day. For `F50` and `F80`, gas accretion is partly halted by ionization feedback from the protostar but the protostar can grow up to $\sim 100\ \mathrm{M}_{\odot}$ with a sufficiently large accretion rate $\sim 10^{-3}\ \mathrm{M}_{\odot}/\mathrm{yr}$ (Fukushima et al. in prep.). The massive star will explode as a SN and contribute to the enrichment of the succeeding generation of stars.

We should also note that the accretion disks forming around the protostars are in most cases gravitationally unstable to fragment (Turk et al. 2009; Clark et al. 2011; Greif et al. 2012). This *disk fragmentation* can occur even in the primordial clouds. This fragmentation mode is distinctive from *cloud fragmentation* induced by radiative cooling (Chiaki et al. 2016). Although the critical conditions for disk fragmentation are still debated (Chon & Hosokawa 2019; Liao, Turk & Schive 2019; Inoue & Yoshida 2020), Takahashi et al. (2016) find that a spiral arm structure developing in a disk can fragment when its minimum Toomre $Q = c_{\mathrm{s}}\Omega_{\mathrm{epi}}/\pi G\Sigma$ becomes less than 0.6, where Ω_{epi} is the epicyclic frequency and Σ is the column density in the perpendicular direction of the disk. For `F50`, spiral arms developed (Fig. 13). We estimate the Toomre Q parameter by approximating $\Omega_{\mathrm{epi}} = 2\Omega$, where Ω is the gas angular momentum, and we find that Q in the spiral arms is below 0.6 (blue colored region in the upper right panel of Fig. 13), which suggests that the arms will fragment. However, since the gas accretion rate onto the protostar is higher ($\sim c_{\mathrm{s}}^3/G \sim 3\times10^{-3}\ \mathrm{M}_{\odot}/\mathrm{yr}$) than in present-day star-forming regions ($\sim 10^{-5}\ \mathrm{M}_{\odot}/\mathrm{yr}$), disk fragmentation might result in the formation of a massive star cluster.

It is numerically challenging to follow the entire accretion process ($\sim 10^5$ yr) because the computational timestep becomes extremely short ($\lesssim$ yr) to meet the Courant condition of the dynamics of dense protostellar cores. In order to follow the late phases of accretion and disk fragmentation, in a future study, we will continue the simulations by using additional numerical techniques such as sink particles, with which the dense region is masked and replaced with Lagrangian particles.

4.2.4 Formation of EMP stars with peculiar abundances

In this series of papers, we have investigated the formation processes of C-normal and CEMP-no stars. For the formation of other classes of EMP stars, additional nucleosynthesis mechanisms are required to be considered. First, s-process elements enhancement of CEMP-s (CEMP Group I) stars can be explained by the binary mass transfer from companion stars in the asymptotic giant branch (AGB) phase (Suda et al. 2004; Komiya et al. 2020). Since the progenitors are low-mass (1–7 $\mathrm{M}_{\odot}$), the companion stars begin to contribute to the enrichment in more massive and metal-rich halos ($[\mathrm{Fe/H}] \gtrsim -3$; Fig. 14) than MHs. Therefore, to see the evolution of low-mass stars and effect of binary transfer, it is required to extend our simulations spatially and temporarily.

Also, rotating stars (“spinstars”) can produce lighter elements (C–Al) and trans-iron elements in their envelopes (Meynet et al. 2006; Choplin & Hirschi 2020). The envelopes are blown away by SN explosions and contribute to C and s-process element enhancement (Choplin, Tominaga & Ishigaki 2019). Since rotating stars also produce nitrogen, the formation of N-enhanced stars such as CS $22952-015$ and BS $16550-087$ could be explained with the spinstar models. Some spinstars are considered to be associated with jet-like SNe (Tominaga 2009). This aspherical explosion model can reproduce Fe-deficient abundance patterns even with larger explosion energies than spherical explosion models because Fe can fall back onto the compact remnants from the equatorial plane. As a result, the elemental abundances of the ejecta depend on the direction from the jet axis. Ezzeddine et al. (2019) speculate that Zn-enhancement of the star HE $1327-2326$ could be explained by the external enrichment of a cloud in a specific angle range from the jet axis of a SN. We will explore the effect of the aspherical structure of ejecta on the metal enrichment in forthcoming papers.

5 CONCLUSION

CEMP stars, the most iron-poor class of stars, hold fossil records of the chemical enrichment in the early Universe (de Bennassuti et al. 2017), and their origin is still under debate. In this work, we follow the metal enrichment from faint SNe and gravitational collapse of the enriched clouds with high-resolution numerical simulations. We find that C abundance of the clouds is $A(\mathrm{C}) = 3.80$, 5.06, and 4.90 for faint SN models with progenitor masses $M_{\mathrm{PopIII}} = 13$, 50, and 80 $\mathrm{M}_{\odot}$, respectively. These are smaller than the abundance range of observed CEMP stars ($A(\mathrm{C}) > 6$) while the abundance of a cloud enriched by a normal CCSN is consistent with the metallicity range of observed C-normal stars (Paper I). This behavior occurs because the mass of metals produced by faint SNe and the fraction of metals incorporated into the clouds are smaller than in normal CCSN model. We also find that our detailed chemistry/cooling model enables us to follow the entire process of fragmentation. AC grain cooling induces fragmentation of the enriched cloud for model `F13` even with the lowest C abundance $A(\mathrm{C}) = 3.80$. This result indicates that low-mass stars with metallicities $[\mathrm{Fe/H}] \sim -9$ may form through cooling by carbon dust grains produced by faint SNe and re-accreted onto the same MH. Such “giga metal-poor” stars may be observed in the future as a larger number of samples of EMP stars will be collected.

So far $\sim$ 5000 metal-poor stars have been observed. With future observational facilities, Subaru/PFS (Takada et al. 2014) and TMT (Skidmore et al. 2015), samples will increase. To prepare for future surveys, it is urgent to study the origin of metal-poor stars from the theoretical side. We have focused on the formation process of C-normal and CEMP-no stars in this series of papers. The other classes of stars, which show neutron-capture element enhancement and peculiar elemental abundances, are believed to form by multiple types of progenitors. We will extend our numerical model to enable comprehensive studies of their formation processes, while being constrained by large samples of observed metal-poor stars. Such a study should reveal elusive details of the chemical enrichment and star formation in the early Universe.

ACKNOWLEDGMENTS

GC is supported by Research Fellowships of the Japan Society for the Promotion of Science (JSPS). JHW is supported by National Science Foundation grants AST-1614333 and OAC-1835213, and NASA grants NNX17AG23G and 80NSSC20K0520. The simulation was performed with NSF’s XSEDE allocation AST-120046 on the Comet and Stampede2 resources and also on the Georgia Tech PACE compute system. The figures in this paper are constructed with the plotting library MATPLOTLIB (Hunter 2007).

REFERENCES

Abel, T., Bryan, G. L., & Norman, M. L. 2002, Science, 295, 93
Aoki, W., Beers, T. C., Christlieb, N., et al. 2007, ApJ, 655, 492
Asplund, M., Grevesse, N., Sauval, A. J., & Scott, P. 2009, ARA&A, 47, 481
Audouze, J., & Silk, J. 1995, ApJ, 451, L49
Beers, T. C., & Christlieb, N. 2005, ARA&A, 43, 531
Belczynski K., Bulik T., Fryer C. L., Ruiter A., Valsecchi F., Vink J. S., Hurley J. R., 2010, ApJ, 714, 1217
Bromm, V., Coppi, P. S., & Larson, R. B. 1999, ApJ, 527, L5
Bryan G. L., Norman M. L., Stone J. M., Cen R., Ostriker J. P., 1995, CoPhC, 89, 149
Bryan G. L., Norman M. L., 1997, arXiv, astro-ph/9710187
Bryan, G. L., Norman, M. L., O’Shea, B. W., et al. 2014, ApJS, 211, 19
Caffau, E., Bonifacio, P., François, P., et al. 2011, Nature, 477, 67
Cayrel, R., Depagne, E., Spite, M., et al. 2004, A&A, 416, 1117
Clark, P. C., Glover, S. C. O., Smith, R. J., et al. 2011, Science, 331, 1040
Chiaki, G., Marassi, S., Nozawa, T., et al. 2015, MNRAS, 446, 2659
Chiaki, G., Yoshida, N., & Hirano, S. 2016, MNRAS, 463, 2781
Chiaki, G., Tominaga, N., & Nozawa, T. 2017, MNRAS, 472, L115
Chiaki, G., Susa, H., & Hirano, S. 2018, MNRAS, 475, 4378
Chiaki, G., & Wise, J. H. 2019, MNRAS, 482, 3933
Chon S., Hosokawa T., 2019, MNRAS, 488, 2658
Choplin A., Tominaga N., Ishigaki M. N., 2019, A&A, 632, A62
Choplin A., Hirschi R., 2020, arXiv, arXiv:2001.02341
de Bennassuti, M., Schneider, R., Valiante, R., & Salvadori, S. 2014, MNRAS, 445, 3039
de Bennassuti M., Schneider R., Valiante R., Salvadori S., 2015, MNRAS, 451, 2108
de Bennassuti, M., Salvadori, S., Schneider, R., Valiante, R., & Omukai, K. 2017, MNRAS, 465, 926
Draine, B. T., & Bertoldi, F. 1996, ApJ, 468, 269
Efstathiou G., Davis M., White S. D. M., Frenk C. S., 1985, ApJS, 57, 241
Ezzeddine R., et al., 2019, ApJ, 876, 97
Fukushima H., Omukai K., Hosokawa T., 2018, MNRAS, 473, 4754
Graziani L., Salvadori S., Schneider R., Kawata D., de Bennassuti M., Maselli A., 2015, MNRAS, 449, 3137
Greif, T. H., Bromm, V., Clark, P. C., et al. 2012, MNRAS, 424, 399
Hartwig, T., Yoshida, N., Magg, M., et al. 2018, MNRAS, 478, 1795
Hahn, O., & Abel, T. 2011, MNRAS, 415, 2101
Hanawa, T., & Matsumoto, T. 2000, PASJ, 52, 241
Haynes C. J., Kobayashi C., 2019, MNRAS, 483, 5123
Hirano, S., Hosokawa, T., Yoshida, N., et al. 2014, ApJ, 781, 60
Hirano, S., Hosokawa, T., Yoshida, N., Omukai, K., & Yorke, H. W. 2015, MNRAS, 448, 568
Hirano, S., & Bromm, V. 2017, MNRAS, 470, 898
Hosokawa, T., Omukai, K., Yoshida, N., & Yorke, H. W. 2011, Science, 334, 1250
Hosokawa, T., Hirano, S., Kuiper, R., et al. 2016, ApJ, 824, 119
Hunter J. D., 2007, CSE, 9, 90
Inoue S., Yoshida N., 2020, MNRAS, 491, L24
Ishigaki, M. N., Tominaga, N., Kobayashi, C., & Nomoto, K. 2014, ApJ, 792, L32
Ishigaki, M. N., Tominaga, N., Kobayashi, C., & Nomoto, K. 2018, arXiv:1801.07763
Keller, S. C., Bessell, M. S., Frebel, A., et al. 2014, Nature, 506, 463
Kitayama, T., & Yoshida, N. 2005, ApJ, 630, 675
Komiya Y., Suda T., Yamada S., Fujimoto M. Y., 2020, arXiv, arXiv:2001.01420
Kozasa, T., & Hasegawa, H. 1987, Progress of Theoretical Physics, 77, 1402
Krumholz M. R., Klein R. I., McKee C. F., Offner S. S. R., Cunningham A. J., 2009, Sci, 323, 754
Lai, D. 2000, ApJ, 540, 946
Larson, R. B. 1969, MNRAS, 145, 271
Liao W.-T., Turk M., Schive H.-Y., 2019, arXiv, arXiv:1911.07898
Limongi, M., & Chieffi, A. 2012, ApJS, 199, 38
Marassi, S., Chiaki, G., Schneider, R., et al. 2014, ApJ, 794, 100
Marassi, S., Schneider, R., Limongi, M., et al. 2015, MNRAS, 454, 4250
Mayer, M., & Duschl, W. J. 2005, MNRAS, 358, 614
McKee C. F., Ostriker J. P., 1977, ApJ, 218, 148
Meynet G., Ekström S., Maeder A., 2006, A&A, 447, 623
Nomoto K., Tominaga N., Umeda H., Kobayashi C., Maeda K., 2006, NuPhA, 777, 424
Nozawa, T., Kozasa, T., Umeda, H., Maeda, K., & Nomoto, K. 2003, ApJ, 598, 785
Nozawa, T., Kozasa, T., Tominaga, N., et al. 2008, ApJ, 684, 1343
Omukai, K. 2000, ApJ, 534, 809
Omukai, K., Tsuribe, T., Schneider, R., & Ferrara, A. 2005, ApJ, 626, 627
Penston, M. V. 1969, MNRAS, 144, 425

Planck Collaboration, Ade, P. A. R., Aghanim, N., et al. 2016, A&A, 594, A13

Placco, V. M., Beers, T. C., Santucci, R. M., et al. 2018, AJ, 155, 256

Ritter, J. S., Sluder, A., Safranek-Shrader, C., Milosavljević, M., & Bromm, V. 2015, MNRAS, 451, 1190

Ryan, S. G., Norris, J. E., & Beers, T. C. 1996, ApJ, 471, 254

Safranek-Shrader, C., Montgomery, M. H., Milosavljević, M., & Bromm, V. 2016, MNRAS, 455, 3288

Salvadori, S., Schneider, R., & Ferrara, A. 2007, MNRAS, 381, 647

Salvadori S., Ferrara A., Schneider R., Scannapieco E., Kawata D., 2010, MNRAS, 401, L5

Schaerer, D. 2002, A&A, 382, 28

Schneider R., Ferrara A., Natarajan P., Omukai K., 2002, ApJ, 571, 30

Schneider, R., Ferrara, A., Salvaterra, R., Omukai, K., & Bromm, V. 2003, Nature, 422, 869

Schneider, R., Omukai, K., Inoue, A. K., & Ferrara, A. 2006, MNRAS, 369, 1437

Schneider, R., Omukai, K., Bianchi, S., & Valiante, R. 2012a, MNRAS, 419, 1566

Schneider, R., Omukai, K., Limongi, M., et al. 2012b, MNRAS, 423, L60

Skidmore W., TMT International Science Development Teams, Science Advisory Committee T., 2015, RAA, 15, 1945

Skinner D., Wise J. H., 2020, MNRAS.tmp, 126

Smith, B., Sigurdsson, S., & Abel, T. 2008, MNRAS, 385, 1443

Smith B. D., Turk M. J., Sigurdsson S., O'Shea B. W., Norman M. L., 2009, ApJ, 691, 441

Smith, B. D., Wise, J. H., O'Shea, B. W., Norman, M. L., & Khochfar, S. 2015, MNRAS, 452, 2822

Smith, B. D., Bryan, G. L., Glover, S. C. O., et al. 2017, MNRAS, 466, 2217

Suda, T., Aikawa, M., Machida, M. N., Fujimoto, M. Y., & Iben, I., Jr. 2004, ApJ, 611, 476

Suda, T., Katsuta, Y., Yamada, S., et al. 2008, PASJ, 60, 1159

Susa, H., Hasegawa, K., & Tominaga, N. 2014, ApJ, 792, 32

Takahashi, S. Z., Tsukamoto, Y., & Inutsuka, S. 2016, MNRAS, 458, 3597

Takada M., et al., 2014, PASJ, 66, R1

Todini, P., & Ferrara, A. 2001, MNRAS, 325, 726

Tominaga N., 2009, ApJ, 690, 526

Tominaga, N., Iwamoto, N., & Nomoto, K. 2014, ApJ, 785, 98

Truelove, J. K., Klein, R. I., McKee, C. F., et al. 1997, ApJ, 489, L179

Turk, M. J., Abel, T., & O'Shea, B. 2009, Science, 325, 601

Turk M. J., Oishi J. S., Abel T., Bryan G. L., 2012, ApJ, 745, 154

Turk M. J., Smith B. D., Oishi J. S., Skory S., Skillman S. W., Abel T., Norman M. L., 2011, ApJS, 192, 9

Tsuribe, T., & Omukai, K. 2006, ApJ, 642, L61

Umeda, H., & Nomoto, K. 2002, ApJ, 565, 385

Umeda, H., & Nomoto, K. 2003, Nature, 422, 871

Verner D. A., Ferland G. J., Korista K. T., Yakovlev D. G., 1996, ApJ, 465, 487

Wise, J. H., & Abel, T. 2011, MNRAS, 414, 3458

Woodward P., Colella P., 1984, J. Comput. Phys., 54, 115

Yoshida, N., Abel, T., Hernquist, L., & Sugiyama, N. 2003, ApJ, 592, 645

Yoon, J., Beers, T. C., Placco, V. M., et al. 2016, ApJ, 833, 20

Yoon, J., Beers, T. C., Dietz, S., et al. 2018, arXiv:1806.04738